Tectonic controls on Taupo Volcanic Zone geothermal expression: Insights from Te Mihi, Wairakei Geothermal Field

D. D. McNamara[1], S. D. Milicich[2], C. Massiot[2], P. Villamor[2], K. McLean[3], F. Sépulveda[3], and W. F. Ries[4]

[1]Earth, Ocean and Ecological Sciences, University of Liverpool, United Kingdom.

[2]GNS Science, New Zealand.

[3]Contact Energy Ltd., New Zealand.

[4]Institut für Geographie und Regionalforschung, University of Vienna, Austria.

Corresponding author: David McNamara (david.d.mcnamara@nuigalway.ie)

Key Points:

- Fault mapping and borehole imaging provide detail on the structure, stress, and fluid flow architecture of the Te Mihi geothermal area.
- Data analyses reveal intersecting, active, E-W, NE-SW striking, normal fault trends which create a zone of biaxial extension at Te Mihi.
- Regions of biaxial extension contribute to the control of geothermal expression in the Taupo Volcanic Zone.

Abstract

Information on structure, stress, and their inter-relationship is essential for understanding structurally controlled geothermal permeability. Active fault mapping, borehole image analysis, and well testing in the Te Mihi geothermal area, New Zealand allows us to refine structural and fluid flow architecture of this resource. The Te Mihi area is structurally complex, comprising a set of NW dipping master faults containing pervasive SE dipping antithetic and splay structures in their hangingwalls. These faults are also intersected by E-W striking faults. A localized, N-S striking structural trend is also observed at Te Mihi. In consideration with Global Navigation Satellite System velocity vectors, both active NE-SW, and E-W striking faults create biaxial extension at Te Mihi, though the observed NE-SW S_{Hmax} direction suggests contemporary extension is NW-SE dominated. Stress field perturbations coincide with structural complexities like fault splays and intersections, and/or proximity to recently active E-W and NE-SW striking structures. Borehole fluid flow at Te Mihi is concentrated at NW dipping master fault intersections, travel time fractures on acoustic image logs, halo fractures on resistivity image logs, NE-SW and E-W striking fractures, intervals of high fracture density, and spatial concentrations of wide aperture fractures and recently active NE-SW and E-W striking fractures. This study suggests Te Mihi geothermal expression results from biaxial extension evident from active structural trend intersections and the predominance of NE-SW and E-W striking structures within permeable well zones. Biaxial extension is therefore an important control on crustal fluid flow within the Taupo Volcanic Zone and thus geothermal resource delineation.

1 Introduction

Fault and fracture networks are important pathways for circulation of hydrothermal fluids in geothermal resources (Braithwaite et al., 2002; Davatzes & Hickman, 2010; McNamara et al., 2014; Siler et al., 2016; Wilson & Rowland, 2016; Wood et al., 2001). Thus, accurately describing the detailed structure and stress field of a geothermal system is key to constraining the reservoir permeability architecture and improving our ability to predict reservoir response to production and injection (Hernandez et al., 2015; Hyman et al., 2016; Jing et al., 2002; Kissling et al., 2017; Massiot et al., 2017a).

Various relationships between structure, lithology, stress, and fluid flow in both natural and enhanced geothermal systems are regularly identified. Interrelationships between structure density, aperture, length, and connectivity play important roles in geothermal fluid flow (Barton et al., 2013; Kissling et al., 2015; Lee et al., 2011a), with zones of higher fracture connectivity and density, often coinciding with the occurrence of longer and wider fractures, frequently associated with increased permeability (Massiot et al., 2017b; McLean & McNamara, 2011; Philipp et al., 2013; Sheridan & Hickman, 2004). Layering and emplacement of volcanic lithologies is also shown to affect the development of fracture lengths and orientations (Gudmundsson et al., 2002; Massiot et al., 2017c; Nemčok et al., 2007), and thus the structural fluid flow network. Stress field conditions in a geothermal reservoir also play a role in a fracture networks ability to transmit fluid (Davatzes & Hickman, 2010; Yoshioka & Stimac, 2010).

Borehole image logs are a proven tool for subsurface lithological, structural, and stress field characterization, and useful for the identification of structurally controlled geothermal fluid flow (Batir et al., 2012; Genter et al., 1995; Hickman & Davatzes, 2010). In New Zealand, novel acquisition of borehole image data, using a high temperature borehole televiewer (BHTV) or well quenching while logging, has provided the first direct subsurface measurements of geothermal reservoir geology (Halwa et al., 2013; McNamara et al., 2017; Milicich et al., 2018; Milloy et al., 2015; Wallis et al., 2012); insights into fracture origin and evolution (Massiot et al., 2017a); data on reservoir in-situ stress and stress variability (Davidson et al., 2012; McNamara et al., 2015); and data inputs for fracture network statistics of lava flow hosted reservoirs allowing quantification of secondary permeability for numerical fluid flow modeling (Kissling & Massiot, 2017; Massiot et al., 2017d). In addition, new high-resolution digital elevation models (DEM) in New Zealand allow more refined active fault mapping, in particular, allowing better assessment of minor (secondary, antithetic), active structures (Villamor et al., 2017a). Such detailed maps can better define the structural setting of New Zealand geothermal fields.

Here we present for the first time in the Te Mihi geothermal area, a robust characterization of the structure, stress, and fluid flow in this resource. Data from new active fault mapping, analysis of four high quality borehole images, observations of structural and lithological information from drill cuttings and core, well completion test data, and 3D geological visualization of the field are combined for the first time and presented in this study. From this rich dataset, this paper provides detailed characterization and discussion of the relationship between structure, stress, and fluid flow within the Te Mihi region of the Wairakei Geothermal Field, and the most refined, to date, understanding of the nature of the structural fluid flow network in the Te Mihi geothermal region. Finally, based on our interpretation of the data presented here, we provide new insights into tectonic controls on structural fluid transport systems in the Taupo Volcanic Zone (TVZ), New Zealand.

2 Geological Setting

The Wairakei Geothermal Field is located within New Zealand's North Island, in the TVZ, the active, southern portion of the Lau-Havre-Taupo extensional back arc basin (Figure 1). The TVZ formed as a result of westward subduction of the Pacific Plate beneath the North Island (Begg & Mouslopoulou, 2010; Cole & Spinks, 2009; Wilson & Rowland, 2016). The geology of the Te Mihi area of the Wairakei Geothermal Field is presented in summary here but is detailed in other studies (Bignall et al., 2007, 2010; McNamara et al., 2013, 2016; Rosenberg, 2017; Rosenberg et al., 2009).

The Te Mihi sector of the Wairakei Geothermal Field lies in the northwest part of the productive reservoir (Figure 1). The stratigraphy of this area is well documented in a number of publications, and briefly recapped here (Bignall et al., 2010; Rosenberg, 2017; Rosenberg et al., 2009). From bottom to top (Figure 2): Tahorakuri Formation units including volcaniclastic deposits, rhyolite to andesite lavas (e.g., Poihipi and Kaiapo rhyolites), and ignimbrites (e.g., Stockyard ignimbrite); ignimbrite deposits of Whakamaru Group ignimbrite; volcaniclastic deposits, lavas and ignimbrites of the Waiora Formation; volcanic-hydrothermal breccia deposits of Rautehuia Breccia (locally); Huka Falls Formation fine-grained lacustrine deposits; Oruanui Formation ignimbrite deposits; and unconsolidated pumice deposits and alluvium. While not yet penetrated by drilling in the Wairakei Geothermal Field (explored depth interval 0 – 2.8 km), the basement rocks are thought to be Torlesse Terrane greywackes. Te Mihi geological units are variably hydrothermally altered following a trend of increasing alteration rank and intensity with depth (Bignall et al., 2010).

The Wairakei Geothermal Field is underlain by a combination NE-SW to ENE-WSW striking faults and fault- controlled basins (Taupo-Reporoa basin to the NE and Te Mihi basin to the NW), as well as the relicts of caldera structures (Grindley, 1965; Wilson et al., 1984). This geothermal resource also lies within an inferred, NW-SE trending, accommodation zone which offsets the Taupo Rift axis (Rowland & Sibson, 2001; Figure 1). Projection of Hauraki rift structures north of the TVZ, align this inferred NW-SE trending accommodation zone with western margin of the Hauraki Rift (Rowland and Simmons, 2012). Structural orientations in the Wairakei Geothermal Field and its Te Mihi region, observed from a mixture of field mapping, fault trenching, aerial photographic analyses, 3D structural modelling of well data, and microseismicity, gravity, and magnetic studies, are dominated by the NE-SW strike regional trend with minor NW-SE, E-W, and N-S strike orientations (Adams et al., 2003; Alcaraz, 2014; Alcaraz et al., 2010; Grindley, 1982; Hunt, 1991; Langridge et al., 2016; Litchfield et al., 2014; Mordriniak & Studt, 1959; Rosenberg, 2017; Rosenberg et al., 2009; Rogan, 1982; Sépulveda et al., 2013, 2015; Villamor et al., 2014, 2017a; Soengkono & Hochstein, 1992; Stagpoole & Bibby, 1999). Existing analyses of borehole image data from the Wairakei Geothermal Field provides dominant NE-SW fracture strike orientations and subpopulations of E-W, and N-S striking fractures (Massiot et al., 2013; McLean & McNamara, 2011; McNamara et al., 2016). Fracture orientations in these studied wells have been observed to vary across the field, within individual wells, and between different lithologies.

3 Materials and Methods

3.1 Active fault mapping

We have mapped active faults in the Te Mihi area from their geomorphic expression, i.e., the identification of fault scarps that displace young landscape surfaces, and in particular the extensive 25 ka old Oruanui ignimbrite constructional surface and younger valleys incised in that surface (Manville & Wilson, 2004). Previous mapping of faults has relied on modern (post-1990) and vintage (1940-1965) aerial photography, low-resolution DEMs (pixels 5-20 m), and field mapping (Villamor et al., 2015). This study utilizes a high-resolution digital elevation model (pixels <1 m) derived from LiDAR (Light Detection and Ranging) data commissioned by the Waikato Regional Council (July 2009). The survey was acquired from a fixed wing aircraft flying at 1200 m using an Optech ALTM 3100EA LiDAR Senor with a field of view of 20 degrees either side of nadir. The resulting point cloud was within the manufacture specifications of a vertical accuracy of +/- 0.15 m. The point cloud was classified into ground first and intermediate returns using automated routines and the manually edited to increase quality. Bare-earth DEMs and hillshade models with a grid size of 1 m were generated and formed the base for all fault mapping.

3.2 Well geology

The stratigraphy and lithology of the four investigated wells is determined from analysis of drill cuttings (Rosenberg, 2017). Where drill cuttings are unavailable due to circulation losses during drilling, the geology along these wells is inferred from 3D modelling and correlation of geological information to nearby wells (Alcaraz, 2014).

3.3 Borehole image log acquisition and processing

BHTV logs of wells WK261, WK264, and WK266 were acquired using an ABI85 high temperature tool. A resistivity image log was acquired in well WK271 by Schlumberger using the Fullbore Formation Microimager (FMI). Details on the acquisition and processing of each image log can be found in Supplement Text S1. All orientation data presented in this paper are with respect to geographic north and horizontal, after correction for borehole deviation and magnetic declination. All depths in meters below sea level (mRL).

3.4 Borehole image quality, feature classification, and data processing

Image quality assessment, feature classification, and data processing follow Massiot et al. (2015) and are detailed fully in Supplementary Text S1-S2. BHTV image quality in wells WK261, WK264, and WK266 is variable (Supplement Text S2). Good image quality is mainly acquired within rhyolite and andesite units, moderate quality within rhyolite lavas, and variably within ignimbrite lithologies of the Tahorakuri Formation and the Whakamaru Group ignimbrite. Imaged intervals of Waiora Formation consistently display poorest image quality, though some depths are moderate to good. In well WK271 image quality is good, with small intervals of moderate image quality. The only exception is the depth interval between -744 and -926 mRL (Waiora Formation) where image quality significantly decreases due to ovalisation of the borehole. Interpretations of data from depth intervals where image quality is less than moderate are of low confidence.

Feature classification for the BHTV logs follows the system laid out by Massiot et al. (2015) (Supplement Data Set S1). Additional classification used in this work includes Travel time fractures (low amplitude fractures that appear on both amplitude and travel time BHTV images (Figure 3A), and ambiguous features (those difficult to determine whether they are natural or induced; Supplementary Figure S6). Feature classification for the resistivity image log includes natural (conductive and resistive fractures, faults, halo fractures, partial fractures, and halo fractures) and induced (DIFTs and PCFs) features. Halo fractures are conductive fractures with a high resistivity halo around them (Figure 3B). All features, and their properties, from each study well are provided in Supplement Data Set S1.

Maximum horizontal stress (S_{Hmax}) orientations are derived from the azimuth of DITFs (Zoback, 2010; no breakout were identified). DITFs are axial parallel where the angle to the borehole axis (ω) $\leq 10^o$) and en échelon where $\omega \geq 10^o$ (Zoback, 2010). 'Fish-hook' DITFs denote a pair of DITFs (~180º apart) connected across the circumference of the borehole wall in a sigmoidal fashion (Supplementary Figure S7). If a structure (fault or fracture) is observed to facilitate this DITF rotation it is further classified as an active structure.

All structural orientation data undergoes statistical correction to address systematic under-sampling of features subparallel to the borehole axes (Table 2; Hudson & Priest 1983; Massiot et al., 2012; Terzaghi, 1965). In addition, apparent fracture apertures measured at the borehole wall are processed to determine fracture-normal (true) aperture (Cheung, 1999; Davatzes & Hickman, 2010; Lofts & Burke, 1999). Fracture density measurements from borehole imaging are known to be strongly dependent on image quality variation in image logs. As such, fracture density, and variation therein, are only considered for raw data (without correcting for orientation bias) obtained within imaged intervals of moderate to good quality.

3.5 Acquisition and processing of well pressure, temperature, and fluid velocity data

Geothermal wells typically have long open-hole intervals, intersecting discrete zones of permeability. These permeable zones are identified from pressure, temperature, and spinner/fluid velocity (PTS) logs, usually acquired under various injection rates. Results from PTS logs are correlated with image log structural interpretations to attempt to identify structural contributions to permeability in geothermal reservoirs (Davatzes & Hickman, 2010; Massiot et al., 2017b; McLean & McNamara, 2011).

The PTS interpretation method is described in detail in Massiot et al. (2017b) and combines: 1) changes in temperature gradient during injection; 2) changes in temperature gradient during heatup; 3) steps in fluid velocity profiles from spinner data; 4) steps in the ratio of fluid velocity profiles from different injection rates; and 5) observation of the pressure control point during heatup. Permeable zones are classified as “major” when multiple indicators are clearly observed, thus indicate a higher contribution to fluid flow in the borehole, and “minor” otherwise. The interpretation of the location and extent of permeable zones is subsequently made robust by a joint interpretation of PTS and image log data, which improves the coarse resolution and uncertainty associated with interpretation of PTS data alone (Massiot et al., 2017b).

4 Results

4.1 Active fault mapping

The active fault map shows that the Te Mihi sector of the Wairakei Geothermal Field is located at an intersection between two fault sets, one striking 045° and another striking 060-070° (Figure 4). Based on their geomorphic expression, faults within the sets mentioned above are normal dip-slip structures. The fluvial drainage crossing this fault is not laterally displaced, as would be expected if these structures contained a component of strike-slip motion.

Tectonic structure changes substantially along rift strike (NE-SW) in the Te Mihi area (Figure 4). South of the field, close to the Lake Taupo shore (~10 km south), a NW dipping, 045° striking structural trend is dominant, represented by the Kaiapo and Whakaipo faults (Landridge et al., 2016). Both faults have prominent, single fault scarps (120 and 25 m high, respectively) displacing the 25 ka Oruanui ignimbrite (Leonard et al., 2010). The Kaiapo Fault, is fast slipping (1.3 mm/yr) relative to other faults in this region (< 0.5 mm/yr; Stirling et al., 2010). Moving NE towards the Te Mihi area, the Kaiapo and Whakaiapo faults, and their deformation, becomes more spatially distributed. Scarp heights along the main fault traces diminish within the same age geomorphic surface (to 25 and 8 m for Kaiapo and Whakaiapo faults respectively, on the Oruanui ignimbrite surface at ~ 4 km south of the Te Mihi region). Subsidiary faulting is observed in between the major Kaiapo and Whakaiapo faults scarps with strike orientations that vary from 045°, to 020°-030° (dipping E, possibly antithetic to the Kaiapo and Whakaipo faults), and 060°. Some 060° striking faults in this area appear at the east side of, or splay from, the Kaiapo Fault trace (e.g., Karapiti Fault).

Within the Te Mihi region itself, a well-defined 070° fault strike trend appears at its southern end, and larger numbers of short 045° striking faults, and some 030° striking faults further distribute the deformation in this area. The 070° striking faults can be observed to intersect many 045° striking ones. Fault scarps are less defined in this region with heights on the Oruanui ignimbrite surface < 5 m, and a few 030° trending, NW dipping traces with 10-25 m high scarps. The LiDAR coverage stops 1 km north of the field and thus mapping there is not very detailed. However, a review of the 1960's aerial photography suggests that the observed distributed deformation presented here may extend another few kilometers before tipping out. From structural mapping of the larger scale TVZ, faulting and deformation seems to step eastwards to the Aratiatia Fault and northwestwards to the Orakonui Fault (Figure 4).

WK261 and WK266 are located in the footwall of, and close (~100 m) to a 030° trending, 25 m high fault scarp. Moving NE, this fault splays into two traces. The easternmost trace shows a right-lateral step to the east where the fault strike changes to 060° before returning to 030° further NE. The westernmost trace is discontinuous and is cross-cut by secondary, 060° striking, SE dipping faults. All 060° trending faults represent a small asymmetric graben bounded by the major 030° trending splay faults. Well WK271 (deviated to the N) is sited in the northern part of this small graben between two 060° striking faults that dip SE. Well WK264 is located ~150 m north of another small, asymmetric graben feature composed of a set of 045° striking faults, and 200 m south of an 060° striking fault that occurs within the right-lateral step previously mentioned. Some of the faults in this latter graben have been exposed and analyzed with paleoseismic trenches that show recent movement (last movement <1800 ka; Villamor et al., 2015).

4.2 Image log features

In the four study wells, 4391 natural features and 2385 induced features are observed (Table 1). These features are predominantly conductive fractures (80%; FMI log) or low amplitude fractures (~99%; BHTV logs). Few structures were classified as faults. A small proportion (3%) of FMI natural features are halo fractures, and about 18% of the low amplitude fractures are travel time fractures. We interpret the 10% 'ambiguous' features as natural fractures given they are all conductive and have orientations that closely resemble those of the conductive fracture features (Supplement Figure S6).

Stress induced features are dominantly DITF pairs. Wells WK261, WK264, and WK266 only display axial parallel DITFs. The DITFs in well WK271 are 65% axial parallel and 35% en échelon (ω values from 10° to 46°). Well WK271 also contains fish-hook DITFs predominantly within the intervals -1231 to -1271 mRL and -1471 to -1556 mRL, within the Whakamaru Group ignimbrite, and Kaiapo rhyolite units respectively.

4.3 Fracture orientation

Observations of fracture orientation, using datasets corrected for orientation bias, show 79% of fractures have dip magnitudes ≥70º. Table 2 shows the percentage of fractures dip directions in the study wells with the dominant trend being NE-SW striking fractures dipping SE. A notable subordinate fracture population striking E-W (dipping N and S equally) is observed in all wells except WK264 where the E-W striking fracture population dominates. An additional N-S striking subordinate fracture orientation is observed in well WK266, dipping both E and W.

The dominant NE-SW trend is present in all imaged lithological units (Figure 5). In addition, there are subordinate trends. The Waiora Formation in wells WK261, WK264, and the upper interval in WK266 have a high proportion of E-W striking fractures. The Whakamaru Group ignimbrite contains high percentages of S dipping, E-W striking fractures in wells WK261 and WK271, and a subordinate E and W dipping, N-S striking fracture trend in well WK261. The imaged intervals of the five rhyolite units show varied fracture patterns. The Karapiti 2B rhyolite (WK266) is dominated by the NE-SW fracture strike trend, as do the Kaiapo rhyolite bodies imaged at the bottom of wells WK261 and WK271. The rhyolite body at the top of the imaged interval of well WK271 displays a bimodal fracture strike pattern of E-W (dipping S) and N-S (dipping E). The imaged Poihipi rhyolite (WK264) shows fractures striking NE-SW and E-W arranged such that above the andesite unit (which interrupts this rhyolite), fractures predominantly dip N to NW, and beneath the andesite fractures dip mainly SE. The andesite intrusion itself has a bimodal fracture strike population of N-S (dipping E), and E-W (dipping N) striking fractures. Vector azimuth plots of fracture dip direction within each well show variations from the dominant fracture orientation trends at higher resolution than the lithological scale (Supplement Figures S8-S12). Well WK271 is interspersed with depth intervals containing fractures dominantly dipping E, W-NW, and W-SW. Well WK261 contains two lengthy intervals of dominantly N-NW dipping fractures. Fractures along well WK266 shows a dominant S-SE dip direction above -231 mRL, and a dominant NW-W fracture dip direction below -231 mRL. WK264 show intervals of fractures dominantly dipping N-NW, N, NE, W-NW, and E-NE.

4.4 Fracture density

Fracture counts from wells WK261, WK264, WK266, and WK271 provide average fracture densities of 1, 2.2, 0.8, and 3.4 fractures/m respectively. High density intervals in each well, defined where fracture density exceeds the average well density, can be found in all stratigraphic layers (Figure 5). High fracture density intervals were mostly located in tuffs and welded ignimbrites in the Waiora and Tahorakuri formations, and in massive and brecciated intervals within the rhyolite bodies. The highest fracture densities in BHTV and FMI logs are found in rhyolites: 3.4 fractures/m in well WK264), and 6.8 fractures/m (within a 119 m interval incorporating the Kaiapo rhyolite and 29 m of the overlying Tahorakuri Formation) in WK271.

4.5 Fracture aperture

True fracture apertures measured from all four study wells range from <1 mm to 895 mm wide (the latter most likely a zone of highly concentrated fractures not individually distinguishable on the image log). On the FMI log (WK271) 56% of wide aperture fractures (those with apertures >10 mm) are resistive fractures, while on the BHTV logs 67% of wide aperture fractures are low amplitude fractures. Wide aperture fractures are located within all lithologies.

4.6 Stress orientation

As wells WK261 and WK264 are sub-vertical (Supplementary Table S1), and DITFs are borehole-axial ($\omega < 10°$) we can assume that the borehole axis is parallel to the vertical stress (S_v) and that the induced feature measurements represent horizontal stress orientations (Zoback, 2010). Wells WK271 and WK266 are deviated from horizontal (Table 3). The effect of well deviation on the orientation of stress-induced features is generally considered negligible for wells deviated <12° from vertical (Mastin, 1988), and in wells deviated up to 29° in the nearby Rotokawa Geothermal Field (McNamara et al., 2015). Following the same method of error derivation of S_{Hmax} orientation as in McNamara et al. (2015), we find the effect of borehole deviation on DITF azimuth in this study to be small (±10° in WK266 and ±5° for WK271).DITF morphologies are all borehole axial in WK266. In WK271, DITFs are borehole axial, en échelon, and fish-hook, and thus may not strictly indicate S_{Hmax} orientations. Fish-hook DITFs are observed in only two depth intervals, circa -1231 to -1271 mRL and -1471 to -1556 mRL, within the Whakamaru Group ignimbrite, and Kaiapo rhyolite respectively.

S_{Hmax} orientations are NE-SW in wells WK261 and WK264; and NNE-SSW in wells WK271 and WK266 (Figure 6, Table 3). In WK271, S_{Hmax} changes from 035 to 018 at -1227 mRL). Stress field rotations are observed in all four study wells. Of these S_{Hmax} rotations, 53% were observed to be the result of DITFs changing orientation over discrete fractures or clusters of fractures, identifying these as active structures (Figure 7A-B). The orientations of active structures are dominantly striking NE-SW and dipping SE (Figure 7C). Stress perturbations caused by active structures show no lithological preference, with 36% observed within rhyolite units, 27% in tuff units, and 37% in ignimbrite units (Figure 6). The majority of the active fractures are of low amplitude on BHTV logs (74%) or high resistivity on the resistivity image log (83%).

4.7 Fluid flow

The PTS log interpretation shows that there are between 5 and 10 permeable zones in each borehole, ranging from 5 - 120 m long intervals, with one major permeable zone in each well (namely permeable zone #7 in WK261; #5 in WK264; #3 in WK266; and #4 in WK271; Supplement Table S3). In WK264, it was possible to further refine the 125 m-long major permeable zone into 5 sub-intervals.

5 Discussion

5.1 The subsurface structural architecture of Te Mihi

Regardless of fracture origin, reservoir structural fabrics in Te Mihi will be dominated by current tectonics, making all reservoir structures, at least in their modern incarnation, tectonic. We interpret all imaged structures from the studied Te Mihi boreholes as tectonic, mainly because their dominant structural trends are consistent with local and regional tectonic trends, but recognize there is possibly a level of inheritance of primary igneous structures in this tectonic structural fabric.

5.1.1 Structural geometry from active fault and borehole image data

New borehole and mapping data shows that the structural architecture in the Te Mihi area is more complex than previously defined. The Te Mihi area contains steeply dipping (>70°) local faults identified from active fault mapping (Figure 9; this study; Stirling et al., 2012; Villamor et al., 2015, 2017a) and from modelled faults (Figure 2; Alcaraz, 2014). These faults predominantly strike NE-SW and dip NW but the Te Mihi area also contains numerous fault traces striking 030° and 060°, both of which have NW and SE dip directions (Figure 9). The NW dipping faults are identified as master structures in the Te Mihi area (i.e., accommodate more deformation) based on field observations of larger surface offsets on these structures (measured from the Oruanui ignimbrite surface). These NW dipping faults splay from the main, NW dipping Kaiapo Fault trace to the south of the Te Mihi area, which then cross-cuts the 060-090° striking fault traces as they move towards the NE into Te Mihi (Figure 9).

In boreholes, we observe a strong dominance of SE dipping fractures in the Te Mihi subsurface along the four studied wells, a contrast to the dominant NW dipping master faults. Faults are complex zones of tectonic deformation (Faulkner at al., 2010), and normal faults in an extensional setting, such as the Te Mihi region, can be associated with a variety of antithetic substructures (Figure 10 – Option 1) occurring both along strike and at fault tips (horse-tailing), where major faults intersect, and at faults step-overs or bends (Faulds et al., 2011; Nicol et al., 1995; Peacock & Sanderson, 1991). Normal faults can also develop splays as they propagate upwards (Walsh & Watterson, 1991), and in steeply dipping normal faults these splays can sometimes become overturned, displaying reverse displacements with antithetic orientations to the master fault (Sharp et al., 2000; Figure 10 - option 2). This phenomenon has been noted on TVZ from shallow (<10 m) trenching of active faults (Villamor & Berryman, 2001; Villamor et al., 2015). Fault plane/zone morphology can be expected to have variable geometric orientations along dip and strike. As such, steeply dipping normal faults may contain segments that are: a) overlapping, creating depth intervals that may contain concentrations of antithetic structures (Childs et al., 1996; Figure 10 - option 3); or, b) over-steepened such that they have antithetic orientations to the overall dip direction within the main fault plane/zone itself (Figure 10 - option 4).

While options 2 to 4 are plausible in the Te Mihi area, we favor the antithetic structural architecture model (option 1) such that the Te Mihi subsurface is comprised of dominantly NW dipping master faults, with many branching SE dipping antithetic faults in the hangingwall (Figure 9; Figure 10 - option 1). The dominant SE dip direction of subsurface fractures measured from borehole images can be explained by the presence of multiple, SE dipping antithetic faults. These antithetic structures in turn result from: (1) horse-tailing fault termination: the major NW dipping Kaiapo Fault termination as it approaches Te Mihi to the north, splaying into several strands forming an asymmetric graben (similar to the Paeroa Fault in the central Taupo Rift; Berryman et al., 2008); (2) intersections of the Kaiapo Fault with the E-W striking (dipping S) fault trend present within the Te Mihi area; (3) fault step overs: deformation along the Kaiapo Fault steps NE to the Aratiatia Fault and NW to the Orakonui Fault, which have opposite dip directions. Furthermore, an antithetic model is consistent with similar conclusions drawn from datasets elsewhere in the TVZ including borehole image fracture analysis in the nearby Rotokawa Geothermal Field (McNamara et al., 2014), fault mapping across the onshore TVZ (Begg & Mouslopoulou, 2010; Villamor et al., 2017b), and seismic profile interpretation in the offshore TVZ rift, the Whakatane Graben (Lamarche et al., 2006).

Of particular interest in the Te Mihi region is the presence of two contemporaneously active normal fault trends intersecting at oblique angles (maximum intersecting angle of 50°, between faults striking 020° and 070°). No detailed paleoseismic studies exist in Te Mihi area to confirm recent activity on 070° striking normal faults present there. However, these fault strikes have been confirmed as active elsewhere in the Taupo Rift (e.g., Snowgrass Fault: Villamor & Berryman (2006); Highlands Road Fault: Nicol et al., (2010)). We thus consider the observed 070° striking faults in the Te Mihi area as active.

Similar E-W striking structural orientations are observed from studied image logs, and are strikingly apparent within distinct depth intervals of well WK264 (Figures 5 and 6). While no mapped E-W striking faults are close to well WK264, one does exist ~1 km to the south of the well. Additionally, a nearby 3D-modelled fault displays local strike variation via a right-step bend (similar to observed surface faulting) creating a localized E-W striking fault segment near well WK264 (Alcaraz, 2014). Deformation associated with either of these structural features can explain the significant E-W striking fractures in well WK264. It is notable that the proportion of E-W striking fractures relative to NE-SW striking fractures decreases with depth in all study wells (Figure 5). Given all study wells lie within E-W striking, S dipping fault footwalls, this pattern reflects the decreasing influence of these faults on the fracture orientations with depth.

N-S striking fracture populations are also noted within specific depth intervals, especially in well WK271 (Figure 5). The shallow, upper rhyolite unit contains a prominent proportion of N-S striking fractures, which decreases within the Waiora Formation underneath, until they become conspicuously absent in the Whakamaru Group ignimbrite further downhole. N-S striking fault trends are observed across the TVZ (Seebeck et al., 2010; Villamor et al., 2017a), and in the Te Mihi region, a strand of the Kaiapo Fault east of well WK271 displays a N-S striking, W dipping orientation. Additionally, structural mapping presented here, and 3D fault modelling (Alcaraz, 2014) of the area near well WK271 shows fault terminations, splays, and intersections, SE-S dipping antithetic faults, and right-stepping brittle deformation towards the Aratiatia Fault. Such fault intersections are often associated with perturbed stress fields, and as such can generate fracture orientation populations that vary from the expected damage zone structures on a fault (Choi et al., 2016; Fossen & Rotevatn, 2016; Peacock et al., 2017; Tsuji et al., 2014). Further discussion on the presence of this N-S fracture strike trend is continued in section 4.5 to take into account stress field observations.

Finally, NW-SE striking fractures are present in low numbers in all four study wells (Figure 5, Table 2). This fracture set, though small, is important to consider in the broader structural context of the Wairakei Geothermal Field's position within the TVZ. The northern region of the Wairakei Geothermal Field, including Te Mihi, is suggested to overlie an inferred accommodation zone of the Taupo Rift oriented perpendicular to the dominant NE-SW extension direction (Rowland & Sibson, 2001; Figure 1). This accommodation zone is inferred to root onto pre-existing, NW-SE striking, Hauraki Rift basement structures that cross the TVZ. Evidence for the presence of such NW-SE oriented, active, basement structures under the Wairakei Geothermal Field comes from preliminary microseismicity studies in the area (Sépulveda et al., 2013), and observed fault lineaments in basement outcrop outside the rift (a review of which is presented in McNamara et al., 2013, Villamor et al., 2017a, and references therein). However, given the low proportions, centimeter scale, and lack of increasing fracture density with depth of NW-SE striking fractures in rift fill units observed here, and in other TVZ borehole image studies (McNamara et al., 2014; Massiot et al., 2013; Wallis et al., 2013), we suggest that they are unlikely to be related to inherited Hauraki Rift basement structures underlying the Te Mihi region. Instead, we interpret their presence as a consequence of the tectonic structural complexity of the rift fill units.

In summary, the structural architecture at Te Mihi in this study displays a complex set of variably oriented rift structures. The dominant structures consist of NE-SW trending, NW dipping faults and fractures that represent splays from the main Kaiapo Fault to the south. These NE-SW striking faults intersect a secondary E-W striking, S-SE dipping fault trend (e.g., Te Mihi Fault) in the Te Mihi region. The spatial distribution and relative abundances of fracture orientations observed from borehole image logs is directly related to the strike orientation of proximal fault strands, or to zones of structural complexity, e.g., antithetic faults, fault intersections, fault splay points, step-overs, and fault terminations.

5.1.2 High fracture density zones and their relationship to lithology and major faults

Densely fractured intervals (fracture density > average well fracture density) occur in all imaged lithologies in the studied wells (Figure 5). Highly fractured intervals in the Te Mihi subsurface may result from: a) different response of lithology to deformation (including effects from igneous rock emplacement and progressive hydrothermal alteration); and/or b) spatially variable tectonic deformation; and/or c) cumulative damage in older lithological units.

Highly fractured intervals in the rhyolite bodies at Te Mihi may correspond to specific components of a rhyolite lava body (e.g., basal and carapace breccias). Such breccia facies are observed in the rhyolitic Ngongotaha Dome of the TVZ (Ashwell et al., 2013). It remains inconclusive as to how much the emplacement structures of the imaged rhyolite bodies contributes to the presence of dense fracture zones within them, and future image log texture analysis is required, such as presented in Milicich et al. (2018).

Competent lithologies often concentrate brittle deformation. However, non-welded, partially-welded, and brecciated intervals (considered weakly competent rock facies) in the Waiora and Tahorakuri formations, and the Whakamaru Group ignimbrite (Rosenberg, 2017), also contain high fracture density intervals in our data. Hydrothermal alteration within the densely fractured intervals of these units can be responsible for cementation and mineral replacement by hydrothermal quartz and calcite (Rosenberg, 2017). We propose here that the intense hydrothermal alteration to hard, hydrothermal minerals in these ignimbrite units increases their competency, promoting brittle deformation and increasing fracture density (Bruhn et al., 1994; Wyering et al., 2014).

High fracture density zones occur both within and outside of projected fault zone intervals (Figures 5). Only well WK261 shows a strong spatial correlation between high fracture density zones and projected fault intersections. In the Te Mihi subsurface, these high density fracture zones likely represent fault damage zones.

Finally, despite a recognized period of depositional hiatus in this region between the Whakamaru Group ignimbrite (~0.35 Ma) and the Tahorakuri Formation (~1 Ma or older; Rosenberg, 2017), there is no clear trend of increased accumulation of fracturing in the older units (Figure 5).

5.2 The state of stress at Te Mihi

5.2.1 Borehole stress feature morphology

The dominance of DITFs and PCFs (tensile features) over borehole breakouts (compressive features) in observed Te Mihi well stress features is expected as DITFs and PCFs are more commonly expressed in regions of extensional tectonics, wells with a large difference between the borehole fluid temperature and formation temperature (ΔT), under-pressured wells, and wells deviated perpendicular to the S_{Hmax} orientation (Zoback, 2010).

DITF morphology can be a function of well deviation (Peška & Zoback, 1995). Wells WK261, WK264, and WK266 only display borehole axial parallel DITFs. While this is expected in vertical wells (WK261 and WK264), en échelon DITF morphologies are expected in deviated well WK266. Deviated well WK271 shows both borehole axial and en échelon DITF morphologies. Variable DITF morphologies in a borehole can be related to perturbation of the stress field orientation via fracture and fault slip activity (Brudy et al., 1997; McNamara et al., 2015). In this manner, a principle stress direction may be brought in-line with a deviated borehole axis thus generating borehole axial DITFs and vice versa. If this alignment is the case in well WK266 it implies that the majority of structures observed in this well are active in order to perturb the stress field orientation along the entire well.

In WK271 borehole axial DITFs are evenly distributed along the well, while high concentrations of en échelon DITFs are coincident with intervals of increased active fracture density associated with stress field orientation perturbation (Figure 6). We interpret that well WK271 deviation is not high enough to generate en échelon DITFs along the entire well, and en échelon DITFs only develop when the stress field is perturbed by active structures. This suggests that despite well deviations of up to ~20°, borehole axial DITFs will form unless fracture slip perturbs the stress field in the Te Mihi area. Similar observations were made of DITF morphologies at the Rotokawa Geothermal Field (McNamara et al., 2015).

The presence of fish-hook DITFs in well WK271 indicates that the combination of stress magnitudes, stress orientations, and well orientation creates a rapidly varying DITF ω angle around the borehole where it is in tension. As the borehole orientation is similar along the imaged length, the presence of the fish-hook DITFs in these depth intervals is likely due to a change in stress field properties, such as the observed variation in S_{Hmax} orientation at approximately -1227 mRL. It is also possible that aspects of the morphology of the fish-hook DITFs may be influenced by factors such as ash layers in the Whakamaru Group ignimbrite, or flow banding in the rhyolite units, providing a path of least resistance for them to propagate along. However, where lithological layering within these intervals can be noted, the fish-hook DITFs cut across the layers, not along them.

5.2.2 Stress field orientation variation and relationships to faults and fractures

The NE-SW S_{Hmax} orientation in the Te Mihi area is consistent with stress orientations recorded from boreholes across the Wairakei Geothermal Field and the TVZ (Massiot et al., 2013; McLean & McNamara, 2011; McNamara et al., 2017), a dominant NE-SW striking extensional fault trend, and with other methods documenting extensional rates and directions across the TVZ (Darby et al., 2000; Hurst et al., 2002; 2016; Townend et al., 2012; Wallace et al., 2004). Here we discuss the potential causes of stress field perturbations from this trend observed both across the region and with depth.

S_{Hmax} orientations in wells WK264 (046°±18°) and WK261 (043°±12°)) differ from more NNE-SSW S_{Hmax} orientations in wells WK266 and WK271 (035°±14° and 018°±15° respectively; Figure 6).

The S_{Hmax} difference observed between wells WK266 (deviated SE) and WK261 (vertical) which are drilled from the same pad may be due to stress field interactions with deviated WK266. However, most borehole stress features observed in well WK266 occur between -200 and -250 mRL, meaning a S_{Hmax} of 035° in well WK266 may not accurately represent the stress field orientation of this area. Both these wells intersect NW dipping, ~045° striking Kaiapo Fault strands but display no stress rotation associated with these structures and so we rule out recent slip on these faults to explain the observed stress orientation variability here.

A large, active, NNE-SSW striking fault to the east of well WK271 may explain the observed 018° S_{Hmax} orientation here (Figure 6). Well WK271 is located in a region of structural complexity including fault terminations, splays, intersections, and step-overs. Furthermore, the ~14-16° rotation of S_{Hmax} observed along WK271 (N-S < -1227 mRL; NNE-SSW >-1227 mRL; Figure 6) coincides with WK271 intersected a projected fault plane. The structural complexity of this area, and recent slip on the fault plane intersected by WK271 can all be contributing to the observed stress field rotation here. This structurally induced horizontal stress field rotation is likely the reason for an increase in N-S striking fractures in the top interval of the well (<-1227 mRL; Figure 5).

In well WK264 S_{Hmax} orientations range from 007°-084°, in the interval -800 to -1000 mRL within the Poihipi rhyolite, centered on the andesite intrusion (Figure 6). While no fault intersections are apparent at this depth interval, sharp increases in the density of active fractures are clear both above and below the andesite unit (Figure 5). We suggest that emplacement of the intrusive body facilitated contemporaneous slip on fractures within the Poihipi rhyolite surrounding it, resulting in the observed stress field perturbation. Stress field rotations resulting from slip have been noted to last on the scale of months to years (Hardebeck & Okada, 2018). As the age of the intrusion is unknown, we are unable to comment on whether the observed stress field perturbation is preserved from that generated by the intrusive event, or maintained by regular slip on the fractures surrounding the intrusion due to contrasting rock properties between the andesite and surrounding rhyolite.

5.2.3 Depth distribution of active structures in geothermal wells

Active structure density in well WK271 increases with depth, notably below -1227 mRL, within the footwall of the intersected Kaiapo Fault strand. This coincides with a decrease in N-S striking fractures with depth, and a more dominant NE-SW fracture strike trend developing. As the dominant fracture strike trend becomes more parallel to the regional S_{Hmax} with depth more fractures are likely to be critically stressed and thus prone to slip (Barton et al., 1995), increasing active structure density here. Conversely, well WK264 shows dominant fracture strike orientation is more perpendicular to the S_{Hmax} orientation. Despite a consistent NE-SW S_{Hmax} orientation along this well, dominant fracture strike orientations change from E-W in the upper intervals (andesite unit and above) to NE-SW below the andesite. The increase in E-W striking fractures may be due to the presence of regional E-W striking fault segments exerting more influence on fracture network development here. If so, the density of active fractures with depth should show an increase, given the increased alignment of fracture strike with the regional S_{Hmax} orientation. Such a pattern is not apparent (Figure 6), and instead we observe highest densities of recently slipped fractures directly above and below the andesite unit, co-incident with the observed localized stress field perturbation here (Figure 6). This observation supports our earlier interpretation that andesite emplacement induced slip on fractures within the rocks above and below it, generating the observed stress field orientation variability.

5.3 Evidence for bi-axial extension in the TVZ

Global Navigation Satellite System (GNSS) velocity vectors in the Taupo Rift-Forearc region show a clear change from a SE direction within the Taupo Rift to an SSE direction within the forearc (Beavan et al., 2016; Figure 11A), supported by focal mechanism and fault slip data (Seebeck et al., 2014). This observation is suggested to represent transtensional kinematics between the North Island Dextral Fault Belt (NIDFB) and the Taupo Rift, and extensional kinematics in the Taupo Rift itself (Wilson and Rowland, 2016). From the northern shore of Lake Taupo to the Southern part of Okataina Volcanic Centre, the GNSS vector orientation change occurs abruptly at the eastern margin of the Taupo Rift. We suggest here that the eastern margin of the rift is subjected to two coeval extensional process: SE-directed rift extension caused mainly by slab roll back perpendicular to the slab contours (Seebeck et al., 2014, Williams et al., 2013); and a further SSE-NNW directed opening by the forearc pull in an SSE direction (Wallace et al., 2004). We propose that the lateral component of the oblique plate conversion along the Hikurangi margin does not only produce rotation of the fore-arc block and strike-slip in the Axial Fault Belt (as suggested by Wallace et al., 2004), but also normal faulting in the eastern margin of the forearc block.

E-W striking faults appear in the Te Mihi area, a location where major NE-SW striking faults (Kaiapo and Whakaipo faults) terminate and/or laterally step over to other major Taupo Rift faults. Active faults with ENE-WSW to E-W strikes are also found at other locations along the Taupo Rift, and as inherited basement faults immediately outside the rift (Villamor et al., 2017b). Furthermore, at the southern termination of the Taupo Rift, active faults striking ~E-W (070°-085°) may reactivate parallel mapped basement faults immediately to the east, where radial extension creates a complex stress and strain field at the rift termination (Villamor & Berryman, 2006). E-W faults are also present along the southern margin of the Okataina Volcanic Centre (Villamor et al., 2017b) and sections of the 1987 ML 6.3 Edgecumbe normal fault surface rupture (Beanland et al., 1989). Secondary faulting with E-W strike trends is mapped in the Ngakuru Graben (~ 20 km south of Rotorua) on the footwall of the Paeroa Fault, and inferred to continue to the west into the graben axis (Downs et al., 2014). The presence of coeval active normal faults at these locations suggests that extension is not uniaxial within parts of the Taupo Rift given none of these fault sets show significant strike-slip components (Seebeck et al., 2014).We propose that, in the region between the NIDFB and the Taupo Rift, and within regions of the Taupo Rift itself, the rotation of the forearc of the Hikurangi margin is partially accommodated by extension on both ENE-WSW to E-W striking faults, instead of transtensional motion. Villamor et al. (2017a) show preliminary mapping of ENE-WSW to E-W striking, active, and potentially active faults in this region that connect both the NIDFB and Taupo Rift fault belts (Figure 11B). E-W fault trends are also common in the basement of this region, in particular in the Axial Ranges (Lee et al., 2011b; Leonard et al., 2010). As ENE-WSW to E-W striking faults hit the eastern margin of the Taupo Rift, they interact and intersect with the dominant NE-SW striking faults there creating coexisting NW-SE and NNW-SSE directed extension (Figure 11B). We thus propose that the ENE-WSW to E-W striking faults in the TVZ are reactivated after the NE-SW striking, normal faulting migrated from the eastern margin of the Old Taupo Rift (Villamor et al., 2015) to its current location (i.e., the Aratiatia Fault at the Te Mihi latitude).

Two coeval pulling forces may also produce local changes in stress field orientations, with stress directions aligning themselves to whichever active structure is most proximal. Te Mihi borehole image data clearly shows a dominant stress field orientation of NW-SE directed extension with only small well-scale variations. This suggests that: 1) the NW-SE extension is the dominant component of extension over the wider Te Mihi area and the NNE-SSW directed extension component is small; or 2) the wells are not close enough to the E-W striking Te Mihi Fault to be substantially affected any reorientation of the stress field. The distance of the main traces of Te Mihi Fault to the study wells is 530 - 1080 m (Figure 8), which suggest that the influence of the E-W trending zones over the main stress field could be localized. However, Massiot et al. (2013) report a NNW-SSE oriented extension direction from borehole image logging in well TH19 in the Tauhara Geothermal Field, SE of the region in this study, suggesting that larger field-scale stress orientation variations do exist.

5.4 Structural controls on permeability in the Te Mihi region: Implications for focused fluid flow in the TVZ

Permeable zones resolution from PTS logging is insufficient to isolate individual structures as fluid conduits but general characteristics of the structural fluid flow pathway can be assessed (Massiot et al., 2017b). Mapped and modelled NW dipping master faults (using dip projects of 70°) in Te Mihi intersect permeable intervals of the four study wells and so we interpret these structures as fluid flow conduits (Figure 8). Further permeable zones can be seen in both hanging and footwalls of these master faults suggesting circulating hydrothermal fluids within fault strands and damage zones.

From BHTV logs it is clear that travel-time fractures, which can be interpreted as open (at least at the borehole wall) cluster within permeable zones (Figure 8) and so we interpret them as part of an open, connected fluid flow network. Fractures classified as 'halo' structures in well WK271 also cluster within permeable zones (Figure 8). These structures can be interpreted as: 1) fractures filled or partially filled with a highly conductive mineral (e.g., pyrite or magnetite; Adams & Dart, 1998; Halwa et al., 2013; Luthi, 2001); 2) a fluid filled fracture, i.e., a highly conductive fracture fill (Lofts & Bourke, 1999; Vasvari, 2011); or 3) a fracture with an alteration zone within the fracture walls resulting from hydrothermal fluid-rock interaction (Long et al., 1996). All interpretations imply that FMI log halo structures are, or were previously, part of a fluid flow structural network, as such we interpret those observed at Te Mihi within permeable zones as part of the current permeable structure network, and those outside the permeable zones as sealed, former fluid conduits. Halo structures are also more concentrated in the permeable zones located in the hangingwall (Figure 8; below the Kaiapo Fault intersection depth interval) suggesting concentrated fluid circulation there, a common observation in extensional faults (Zhang & Sanderson, 1996).

Recently active structures are potential fluid flow conduits (Barton et al., 1995). In all four wells, permeable zones coincide with increases in active structures density and/or intervals of significant stress field orientation variation, though not all (Figures 7 and 8). Furthermore, fractures that display wide apertures preferentially lie within the observed permeable zones, as do 69% of the identified intervals of high fracture density in general (Figure 8). Thus, we interpret wide aperture, recently active, and high density zone fractures to be part of the structural fluid flow network in Te Mihi. Fracture orientations in permeable zones are similar to overall orientation trends with a few exceptions (Figure 8). In well WK264 fractures in permeable zone dominantly dip SSE, while fractures outside the permeable zones have dominant NW, W, and SE dip directions. As discussed, fractures dipping S-SSE are related to a nearby E-W striking, S-dipping kink in an otherwise NE-SW, NW dipping regional fault. Such structural complexity is frequently associated with geothermal permeability in extensional tectonics (Faulds et al., 2010; 2013). While a NE-SW strike trend is identified for permeable zone fractures, it is important to note that the same fracture orientations are observed external to the permeable zones. Thus, fracture orientation alone is not enough to identify permeable structures in Te Mihi. Fractures outside of permeable zones may be impermeable for reasons that include; a lack of connectivity to the larger circulating structural network, or hydrothermal mineral deposition resulting in fracture sealing.

Our proposed 'biaxial' (NW-SE and NNW-SSE) extension experienced within the TVZ can produce enhanced dilation locally and thus generate significant fault permeability. Within uniaxial extensional fields, the presence of an intersecting active fault network can explain large permeability where changes in fault azimuth or dip (dilatational jogs), fault intersections, step-overs, and fault terminations occur (Curewitz & Karson, 1997; Maerten et al., 2002; Sibson, 1996). Similar features are observed at many locations along the Taupo Rift (Rowland & Sibson, 2001; Rowland & Simmons, 2012; Villamor et al., 2017b) and likely contributes to permeability in the Te Mihi area too. However, based on structural and stress results, we suggest that the coexistence of two oblique pulling forces creates special conditions that determine sites like Te Mihi to be more permeable than other fault intersections in the rift, and thus more prone to host geothermal activity.

Numerical experiments suggest that in fault networks, slip on one fault consistently opens fractures at nearby fault intersections (Sanderson & Zhang, 1999). In the Te Mihi case, because both fault trends are active, the level of fracturing during fault rupture will be substantial from repeated rupture of both fault sets, or perhaps from combined rupture. In 1980, Horsfield demonstrates that contemporaneous movement along crossing conjugate normal faults with mutual offset leads to generation of new fault segments, and a complex interference structural pattern. That study could be considered an analogue to the intersection between the Kaiapo and Te Mihi faults where we have shown a complex interference structural pattern both from mapping and borehole data analysis.

How these sites of biaxial stress enhanced permeability link to proposed permeability enhancement at TVZ-Hauraki Rift structural intersections deeper in the basement bears further examination. As stated, borehole studies across the TVZ suggests little influence on geothermal fluid flow from NW-SE oriented structures within rift fill units, and also within greywacke basement units studied in the Kawerau Geothermal Field (Wallis et al., 2012). However, this does not rule out the potential for TVZ-Hauraki Rift structural intersections to act as a deeper focus for upwelling of geothermal fluids through the basement, which is then directed into flow paths facilitated by NE-SW and E-W striking fault interactions in the rift fill. Further work should investigate the contributing influences of subduction processes and combined deep basement and rift fill fault intersections on the 3D-spatial distribution of geothermal fields, as well as the influence, if any, of inherited basement structures on the development of NE-SW and E-W fault intersections within the rift. While the geometry and kinematics of these types of intersections, and their relationship to the wider plate kinematics needs further study, we point here to the possibility that the E-W trending active faults in the Taupo Rift could become a geothermal prospecting target.

6 Conclusions

This study resolves details of the Te Mihi area's complex structural architecture. Faults mapped on surface and fractures mapped on borehole images dominantly strike NE-SW, intersected by a secondary concentration of E-W striking structure in the region. We interpret the region to be dominated by NW dipping master faults containing pervasive S-SE dipping antithetic faults and splays (horse-tailing) within their hangingwalls, evidenced by image log fracture distribution patterns. Intersecting E-W striking faults dip S, and fracture patterns suggest the presence of N dipping antithetic structures and splays in their hangingwalls. The dominant S_{Hmax} orientation is NE-SW. Localized stress field orientation perturbations occur between and along wells which are attributed to either (1) spatial correlation with zones of structural complexity and/or (2) recent slip on proximal regional faults, or across discrete fractures.

Structural controls on borehole fluid flow at Te Mihi are identified and consist of NW dipping master fault intersections, depth intervals of high fracture density, concentrations of travel-time fractures (BHTV) and halo fractures (FMI), NE-SW and E-W striking active structures, and wide aperture fractures. The intersecting NE-SW and E-W striking active normal faults suggest Te Mihi lies within a region of biaxial extension, likely due to the changing plate motion vectors, from NW-SE in the western TVZ towards an N-S direction at the eastern TVZ boundary, nearer the NIDFB. However, the dominant NE-SW S_{Hmax} direction recorded here, concurrent with the regional TVZ trend, implies that NW-SE extension direction is dominant. Concentration of geothermal expression at Te Mihi is thus proposed to be a product of enhanced permeability from the dual extension directions in the area. This is supported by the prevalent NE-SW and E-W striking fracture orientations found within Te Mihi well permeable zones. Other such zones of similar structural intersection exist within the TVZ suggesting this tectonic process may, in part, control geothermal expression distribution.

Acknowledgments, Samples, and Data

The authors would like to acknowledge GNS Science and the New Zealand Ministry Business, Innovation and Employment for providing funding for this study through the New Zealand Geothermal Future research program. We also thank Contact Energy for the acquisition and contribution of the raw image log datasets utilized in the study, and for access to the 3D geological model of the reservoir. Contact Energy Ltd. own and manage access to raw image logs, well test data, and 3D geological models used in the study. Thanks to the Waikato Regional Council for provision of LiDAR data used in this study. Much appreciation goes to Dr Mark Lawrence for feedback and commentary on this manuscript. The authors also acknowledge support of this work by Haliburton Software and Services, a Haliburton Company through the use of Recall™ Borehole software.

References

Adams, J. T., & Dart, C. (1998). The appearance of potential sealing faults on borehole images. Geological Society, 147(1), 7186. http://doi.org/10.1144/GSL.SP.1998.147.01.05

Alcaraz, S. A. (2014). Update to the Wairakei-Tauhara 3-D geological model. GNS Science consultancy report 2014/113LR.

Alcaraz, S. A., Sépulveda, F., Lane, R., Rosenberg, M. D., Rae, A. J., & Bignall, G. (2010). A 3-D representation of the Wairakei geothermal system (New Zealand) using "earth research" geothermal visualisation and modelling software. Transactions Geothermal Resources Council, 34, 1020–1024.

Ashwell, P. A., Kennedy, B. M., Gravley, D. M., von Aulock, F. W., Cole, J. W. (2013). Insights into caldera and regional structures and magma body distribution from lava domes at Rotorua Caldera, New Zealand. Journal of Volcanology and Geothermal Research, 258, 187–202. http://doi.org/10.1016/j.jvolgeores.2013.04.014

Barton, C. A., Moos, D., Hartley, L., Baxter, S., Foulquier, L., Holl, H., & Hogarth, R. (2013). Geomechanically coupled simulation of flow in fractured systems (pp. 1–12). Paper presented at 38th Workshop on Geothermal Reservoir Engineering, Stanford, U.S.A.

Barton, C. A., Zoback, M. D., & Moos, D. (1995). Fluid flow along potentially active faults in crystalline rock. Geology, 23(8), 683-686.

Batir, J., Davatzes, N. C., & Asmundsson, R. (2012). Preliminary model of fracture and stress state in the Hellisheidi Geothermal Field, Hengill Volcanic System, Iceland. Paper presented at 37th Workshop on Geothermal Reservoir Engineering, Stanford, U.S.A.

Beanland, S., Berryman, K. R., & Blick, G. H. (1989). Geological investigations of the 1987 Edgecumbe earthquake, New Zealand. New Zealand journal of geology and geophysics, 32(1), 73-91.

Beavan, J., Wallace, L.M., Palmer, N., Denys, P., Ellis, S., Fournier, N., Hreinsdottir, S., Pearson, C. & Denham, M. (2016). New Zealand GPS velocity field: 1995–2013. New Zealand Journal of Geology and Geophysics, 59, 5-14.

Begg, J. G., & Mouslopoulou, V. (2010). Analysis of late Holocene faulting within an active rift using LIDAR, Taupo Rift, New Zealand. Journal of Volcanology and Geothermal Research, 190(1), 152–167. http://doi.org/10.1016/j.jvolgeores.2009.06.001

Berryman, K., Villamor, P., Nairn, I., Van Dissen, R., Begg, J., & Lee, J. (2008). Late Pleistocene surface rupture history of the Paeroa fault, Taupo rift, New Zealand. New Zealand Journal of Geology and Geophysics, 51(2), 135-158.

Bignall, G., Milicich, S. D., Ramirez, E., Rosenberg, M. D., Kilgour, G., & Rae, A. J. (2010). Geology of the Wairakei-Tauhara Geothermal System, New Zealand (pp. 1–8). Paper presented at World Geothermal Congress, Bali, Indonesia.

Bignall, G., Rosenberg, M. D., Kilgour, G., Milicich, S. D., & Rae, A. J. (2007). Stratigraphy of the western Wairakei Geothermal Field: insights from recent drilling in the greater Te Mihi area (pp. 1–8). Paper presented at 29th New Zealand Geothermal Workshop, New Zealand.

Braithwaite, R.L., Wood, C.P., Rosenberg, M.D. & Faure, K. (2002). Porosity and permeability in the basement rocks at the Kawerau and Ohaaki geothermal fields, New Zealand. In Proceedings of the 24th New Zealand Geothermal Workshop (pp. 49-54).

Brudy, M., Zoback, M. D., Fuchs, K., Rummel, F., & BaumgäRtner, J. (1997). Estimation of the complete stress tensor to 8 km depth in the KTB scientific drill holes: Implications for crustal strength. Journal of Geophysical Research: Solid Earth, 102 (B). http://doi.org/10.1029/96JB02942

Bruhn, R. L., Parry, W. T., Yonkee, W. A., & Thompson, T. (1994). Fracturing and hydrothermal alteration in normal fault zones. Pure and Applied Geophysics, 142, 609-644, https://doi.org/10.1007/BF00876057

Cheung, P. S. (1999). Microresistivity and ultrasonic imagers: tool operations and processing principles with reference to commonly encountered image artefacts. Geological Society, 159(1), 45–57. http://doi.org/10.1144/GSL.SP.1999.159.01.02

Childs, C., Nicol, A., Walsh, J. J., & Watterson, J. (1996). Growth of vertically segmented normal faults. Journal of Structural Geology, 18(1), 1389–1397. http://doi.org/10.1016/S0191-8141(96)00060-0

Choi, J.-H., Edwards, P., Ko, K., & Kim, Y.-S. (2016). Definition and classification of fault damage zones: A review and a new methodological approach. Earth Science Reviews, 152, 70–87. http://doi.org/10.1016/j.earscirev.2015.11.006

Cole, J. W., & Spinks, K. D. (2009). Caldera volcanism and rift structure in the Taupo Volcanic Zone, New Zealand. Geological Society, London, Special Publications, 327(1), 9–29. http://doi.org/10.1144/SP327.2

Curewitz, D., & Karson, J. A. (1997). Structural settings of hydrothermal outflow: Fracture permeability maintained by fault propagation and interaction. Journal of Volcanology and Geothermal Research, 79(3-4), 149-168.

Darby, D. J., K. M. Hodgkinson, & Blick, G. H. (2000). Geodetic measurement of deformation in the Taupo Volcanic Zone, New Zealand: The north Taupo network revisited, New Zealand Journal of Geology and Geophysics, 43(2), 157–170.

Davatzes, N., & Hickman, S. H. (2010). Stress, fracture, and fluid-flow analysis using acoustic and electrical image logs in hot fractured granites of the coos geothermal field, California, U.S.A. AAPG Memoir, (92), 259–293. http://doi.org/10.1306/13181288M923134

Davidson, J., Siratovich, P., Wallis, I., Gravley, D., & McNamara, D.D. (2012). Quantifying the stress distribution at the Rotokawa Geothermal Field, New Zealand. Paper presented at 34th New Zealand Geothermal Workshop, Auckland, New Zealand.

Downs, D. T., Rowland, J. V., Wilson, C. J. N., Rosenberg, M. D., Leonard, G. S., & Calvert, A. T. (2014). Evolution of the intra-arc Taupo-Reporoa Basin within the Taupo Volcanic Zone of New Zealand. Geosphere, 10(1), 185-206.

Faulds, J.E., Hinz, N.H., Coolbaugh, M.F., Cashman, P.H., Kratt, C., Dering, G., Edwards, J., Mayhew, B. & McLachlan, H., (2011). Assessment of favorable structural settings of geothermal systems in the Great Basin, western USA. Geothermal Resources Council Transactions, 35, pp.777-783.

Faulds, J., Coolbaugh, M., Bouchot, V., Moek, I., & Oguz, K. (2010). Characterizing Structural Controls of Geothermal Reservoirs in the Great Basin, USA, and Western Turkey: Developing Successful Exploration Strategies in Extended Terranes. Paper presented at World Geothermal Congress, Bali, Indonesia.

Faulds, J. E., Hinz, N. H., Dering, G. M., & Siler, D. L. (2013). The hybrid model–the most accommodating structural setting for geothermal power generation in the Great Basin, western USA. Geothermal Resources Council Transactions, 37, 3-10.

Faulkner, D. R., Jackson, C. A. L., Lunn, R. J., Schlische, R. W., Shipton, Z. K., Wibberley, C. A. J., & Withjack, M. O. (2010). A review of recent developments concerning the structure, mechanics and fluid flow properties of fault zones. Journal of Structural Geology, 32(11), 1557–1575. http://doi.org/10.1016/j.jsg.2010.06.009

Fossen, H., & Rotevatn, A. (2016). Fault linkage and relay structures in extensional settings—A review. Earth Science Reviews, 154, 14–28. http://doi.org/10.1016/j.earscirev.2015.11.014

Genter, A., Traineau, H., Dezayes, C., Elsass, P., Ledesert, B., Meunier, A., & Villemin, T. (1995). Fracture analysis and reservoir characterization of the granitic basement in the HDR Soultz Project (France). Geothermal Science and Technology, 4(3), 189–214. http://doi.org/10.1016/0148-9062(96)83915-5

Geographx (2012). NZ 8m Digital Elevation Model (2012), created by Geographx (http://geographx.co.nz) and released under Creative Commons Attribution 4.0 International.

Grindley, G. W. (1965). The geology, structure, and exploitation of the Wairakei geothermal field. New Zealand Geological Survey Bulletin, 75.

Grindley, G. W. (1982). The deeper structure of the Wairakei Geothermal Field. Paper presented at Pacific Geothermal Conference, Lower Hutt, New Zealand.

Gudmundsson, A., Fjeldskaar, I., & Brenner, S. L. (2002). Propagation pathways and fluid transport of hydrofractures in jointed and layered rocks in geothermal fields. Journal of Volcanology and Geothermal Research, 116(3-4), 257–278. http://doi.org/10.1016/s0377-0273(02)00225-1

Halwa, L., Wallis, I. C., & Lozada, G. T. (2013). Geological analysis of the volcanic subsurface using borehole resistivity images in the Ngatamariki Geothermal Field, New Zealand. Paper presented at 35th New Zealand Geothermal Workshop, Rotorua, New Zealand.

Hardebeck, J. L., & Okada, T. (2018). Temporal stress changes caused by earthquakes: A review. Journal of Geophysical Research: Solid Earth, 123(2), 1350-1365.

Hernandez, D., Clearwater, J., Burnell, J., Franz, P., Azwar, L., & Marsh, A. (2015). Update on the modeling of the Rotokawa geothermal system: 2010–2014. Paper presented at World Geothermal Congress, Melbourne, Australia.

Hickman, S., & Davatzes, N. C. (2010). In-situ stress and fracture characterisation for planning an EGS stimulation in the Desert Peak Geothermal Field, Nevada. Paper presented at 35th Workshop on Geothermal Reservoir Engineering, Stanford, U.S.A.

Horsfield, W. T. (1980). Contemporaneous movement along crossing conjugate normal faults. Journal of Structural Geology, 2, 305-310.

Hudson, J. A., & Priest, S. D. (1983). Discontinuity frequency in rock masses. International Journal of Rock Mechanics and Mining Sciences, 20(2), 73–89. http://doi.org/10.1016/0148-9062(83)90329-7

Hunt, T. M. (1991). Gravity anomaly map of Wairakei Geothermal Field, Geology and Geophysics Division, New Zealand Department of Scientific and Industrial Research, Contract Report 1991/1, Wellington, New Zealand.

Hurst, A. W., Bibby, H. M., Robinson, R. R. (2002). Earthquake focal mechanisms in the central Taupo Volcanic Zone and their relation to faulting and deformation. New Zealand Journal of Geology and Geophysics, 45(4), 527–536. http://doi.org/10.1080/00288306.2002.9514989

Hurst, T., Heise, W., Hreinsdottir, S., & Hamling, I. (2016). Geophysics of the Taupo Volcanic Zone: A review of recent developments. Geothermics, 59, 188-204.

Hyman, J. D., Aldrich, G., Viswanathan, H., Makedonska, N., & Karra, S. (2016). Fracture size and transmissivity correlations: Implications for transport simulations in sparse three-dimensional discrete fracture networks following a truncated power law distribution of fracture size. Water Resources Research, 52(8), 6472–6489. http://doi.org/10.1002/2016WR018806

Jing, Z., Watanabe, K., Willis-Richards, J., & Hashida, T. (2002). A 3-D water/rock chemical interaction model for prediction of HDR/HWR geothermal reservoir performance. Geothermics, 31(1), 1-28.

Kissling, W. & Massiot, C. (2017). Geometrical modelling of fracture networks in an andesite-hosted geothermal reservoir. Paper presented at 39th New Zealand Geothermal Workshop, Rotorua, New Zealand.

Kissling, W. M., Ellis, S. E., McNamara, D. D., Massiot, C. (2015). Modelling fluid flow through fractured rock: Examples using TVZ geothermal reservoirs. Paper presented at 37th New Zealand Geothermal Workshop, Taupo, New Zealand.

Lamarche, G., Barnes, P. M., & Bull, J. M. (2006). Faulting and extension rate over the last 20,000 years in the offshore Whakatane Graben, New Zealand continental shelf. Tectonics, 25(4). http://doi.org/10.1029/2005TC001886

Langridge, R. M., Ries, W. F., Litchfield, N. J., Villamor, P., Van Dissen, R. J., Barrell, D., et al. (2016). The New Zealand Active Faults Database. New Zealand Journal of Geology and Geophysics, 59(1), 86–96. http://doi.org/10.1080/00288306.2015.1112818

Lee, C.-C., Lee, C.-H., Yeh, H.-F., & Lin, H.-I. (2011a). Modeling spatial fracture intensity as a control on flow in fractured rock. Environmental Earth Sciences, 63(6), 1199–1211. http://doi.org/10.1007/s12665-010-0794-x.

Lee, J. M., Townsend, D., Bland, K., Kamp, P. J. J. (2011b). Geology of the Hawke's Bay area: scale 1:250,000. Institute of Geological & Nuclear Sciences 1:250,000 geological map 8.

Leonard, G. S., Begg, J. G., Wilson, C. J. J. (2010). Geology of the Rotorua area: scale 1:250,000. Institute of Geological & Nuclear Sciences Limited 1:250,000 geological map 5.

Litchfield, N.J., Van Dissen, R., Sutherland, R., Barnes, P.M., Cox, S.C., Norris, R., Beavan, R.J., Langridge, R., et al. (2014). A model of active faulting in New Zealand. New Zealand Journal of Geology and Geophysics, 57(1), pp.32-56.

Lofts, J. C., & Bourke, L. T. (1999). The recognition of artefacts from acoustic and resistivity borehole imaging devices. Geological Society, London, Special Publications, 159(1), 59–76. http://doi.org/10.1144/gsl.sp.1999.159.01.03

Long, J.C.S., Aydin, A., Brown, S.R., Einstein, H.H., Hestir, K., Hsieh, P.A., Myer, L.R., Nolte, K.G., et al. (1996). Rock Fractures and Fluid Flow, Contemporary Understanding and Applications, National Academy Press, Washington, D. C., 551 pp

Luthi, S. (2001). Geological well logs: Their use in reservoir modeling. Springer Science Business Media.

Maerten, L., Gillespie, P., & Pollard, D.D. (2002). Effects of local stress perturbation on secondary fault development. Journal of Structural Geology, 24(1), pp.145-153.

Manville, V. & Wilson, C.J. (2004). The 26.5 ka Oruanui eruption, New Zealand: A review of the roles of volcanism and climate in the post-eruptive sedimentary response. New Zealand Journal of Geology and Geophysics, 47, 525-547.

Mardia, K.V. (1972). Statistics of orientation data, Academic Press, London

Massiot, C., McNamara, D., Lewis, B., Price, L., & Bignall, G. (2012). Statistical corrections of fracture sampling bias in boreholes from acoustic televiewer logs. Paper presented at New Zealand Geothermal Workshop, Auckland, New Zealand.

Massiot, C., McNamara, D. D., & Lewis, B. (2013). Interpretive review of the acoustic borehole image logs acquired to date in the Wairakei-Tauhara Geothermal Field, GNS Science Report, 2013/04.

Massiot, C., McNamara, D. D., & Lewis, B. (2015). Processing and analysis of high temperature geothermal acoustic borehole image logs in the Taupo Volcanic Zone, New Zealand. Geothermics, 53, 190–201. http://doi.org/10.1016/j.geothermics.2014.05.010

Massiot, C., Nicol, A., McNamara, D. D., & Townend, T. (2017a). Evidence for tectonic, lithologic, and thermal controls on fracture system geometries in an andesitic high-temperature geothermal field, Journal of Geophysical Research: Solid Earth, 122.

Massiot, C., McLean, K., McNamara, D. D., Sépulveda, F., & Milicich, S. D. (2017b). Discussion between a reservoir engineer and a geologist: Permeability identification from completion test data and borehole image logs integration. Paper presented at 39th New Zealand Geothermal Workshop, Rotorua, New Zealand.

Massiot, C., Nicol, A., Townend, J., McNamara, D. D., García-Sellés, D., Conway, C. E., & Archibald, G. (2017c). Quantitative geometric description of fracture systems in an andesite lava flow using terrestrial laser scanner data. Journal of Volcanology and Geothermal Research, 1–17. http://doi.org/10.1016/j.jvolgeores.2017.05.036

Massiot, C., Townend, J., Nicol, A., & McNamara, D. D., (2017d), Statistical methods of fracture characterisation using acoustic borehole televiewer log interpretation, Journal of Geophysical Research: Solid Earth, 122.

Mastin, L. (1988). Effect of borehole deviation on breakout orientations. Journal of Geophysical Research: Solid Earth, 93(B8), 9187-9195.

McLean, K., & McNamara, D. (2011). Fractures interpreted from acoustic formation imaging technology: correlation to permeability. Paper presented at the Thirty-Sixth Workshop on Geothermal Reservoir Engineering, Auckland, New Zealand.

McNamara, D. D., Bannister, S., Villamor, P., Sépulveda, F., Milicich, S., Alcaraz, S., & Massiot, C. (2016). Exploring Structure and Stress from Depth to Surface in the Wairakei Geothermal Field, New Zealand. Paper presented at the 41st Workshop on Geothermal Reservoir Engineering, Stanford, U.S.A.

McNamara, D.D., Massiot, C., & Milicich, S.D. (2017), Characterising the subsurface structure and stress of New Zealand's geothermal fields using borehole images, Energy Procedia, 125, 273-282, 10.1016/j.egypro.2017.08.176

McNamara, D. D., Massiot, C., Lewis, B. (2013). A Structural Review of the Wairakei-Tauhara Geothermal Field. GNS Science Report.

McNamara, D. D., Massiot, C., Lewis, B. (2014). Heterogeneity of structure and stress in the Rotokawa Geothermal Field, New Zealand. Journal of Geophysical Research: Solid Earth, 120, http://doi.org/10.1002/(ISSN)2169-9356

Milicich, S. D., Massiot, C., & McNamara, D. D. (2018). Volcanic texture identification and influence on permeability using a borehole resistivity image log in the Whakamaru Group ignimbrite, Wairakei Geothermal Field, New Zealand. Paper presented at 43rd Workshop on Geothermal Reservoir Engineering, Stanford, U.S.A.

Milloy, S. F., McLean, K., & McNamara, D. D. (2015). Comparing Borehole Televiewer Logs with Continuous Core: An Example from New Zealand. Paper presented at World Geothermal Congress, Melbourne, Australia.

Mordriniak, N., & Studt, F. E. (1959) Geological structure and volcanism of the Taupo-Tarawera district, New Zealand Journal of Geology and Geophysics, 2, 654–684.

Nemčok, M., Moore, J. N., Christensen, C., Allis, R., Powell, T., Murray, B., & Nash, G. (2007). Controls on the Karaha–Telaga Bodas geothermal reservoir, Indonesia. Geothermics, 36 (1), 9-46.

Nicol, A., Walsh, J. J., Watterson, J., & Bretan, P. G. (1995). Three-dimensional geometry and growth of conjugate normal faults. Journal of Structural Geology, 17(6), 847-862.

Nicol, A., Walsh, J. J., Villamor, P., Seebeck, H., & Berryman, K. R. (2010). Normal fault interactions, paleoearthquakes and growth in an active rift. Journal of Structural Geology, 32, 1101-1113.

Peacock, D. C. P., & Sanderson, D. J. (1991). Displacements, segment linkage and relay ramps in normal fault zones. Journal of Structural Geology, 13(6), 721-733.

Peacock, D. C. P., Nixon, C. W., Rotevatn, A., Sanderson, D. J., & Zuluaga, L. F. (2017). Interacting Faults. Journal of Structural Geology, 97, 1–22. http://doi.org/10.1016/j.jsg.2017.02.008

Peška, P., & Zoback, M. D. (1995). Compressive and tensile failure of inclined well bores and determination of in situ stress and rock strength. Journal of Geophysical Research: Solid Earth, 100(B), 12–. http://doi.org/10.1029/95JB00319

Philipp, S., Afşar, F., & Gudmundsson, A. (2013). Effects of mechanical layering on hydrofracture emplacement and fluid transport in reservoirs. Frontiers of Earth Science (Structural Geology and Tectonics), 1, 4. http://doi.org/10.3389/feart.2013.00004

Risk, G. F. (1984). Electrical resistivity survey of the Wairakei Geothermal Field. Paper presented at 6th New Zealand Geothermal Workshop, Auckland, New Zealand.

Risk, G. F. (2000). Electrical resistivity of the Rotokawa Geothermal Field, New Zealand. Paper presented at 22nd New Zealand Geothermal Workshop, Auckland, New Zealand.

Rogan, M. (1982). A geophysical study of the Taupo Volcanic Zone New Zealand. Journal of Geophysical Research: Solid Earth, 87(B), 4073–4088. http://doi.org/10.1029/JB087iB05p04073

Rosenberg, M. (2017). Volcanic and tectonic perspectives on the age and evolution of the Wairakei-Tauhara geothermal system, (Doctoral Dissertation). University of Victoria, Wellington, New Zealand.

Rosenberg, M. D., Bignall, G., & Rae, A. J. (2009). The geological framework of the Wairakei–Tauhara Geothermal System, New Zealand. Geothermics, 38(1), 72–84. http://doi.org/10.1016/j.geothermics.2009.01.001

Rowland, J. V., & Sibson, R. H. (2001). Extensional fault kinematics within the Taupo Volcanic Zone, New Zealand: Soft-linked segmentation of a continental rift system. New Zealand Journal of Geology and Geophysics, 44(2), 271–283. http://doi.org/10.1080/00288306.2001.9514938

Rowland, J. V., & Simmons, S. F. (2012). Hydrologic, magmatic, and tectonic controls on hydrothermal flow, Taupo Volcanic Zone, New Zealand: implications for the formation of epithermal vein deposits. Economic Geology, 107(3), 427–457. http://doi.org/10.2113/econgeo.107.3.427

Seebeck, H., Nicol, A., Stern, T. A., Bibby, H. M., & Stagpoole, V. (2010). Fault controls on the geometry and location of the Okataina Caldera, Taupo Volcanic Zone, New Zealand. Journal of Volcanology and Geothermal Research, 190(1), 136–151. http://doi.org/10.1016/j.jvolgeores.2009.04.011

Sépulveda, F., Andrews, J., Alvarez, M., Montague, T., & Mannington, W. I. (2013). Overview of deep structure using microseismicity at Wairakei. Paper presented at 35th New Zealand Geothermal Workshop, Rotorua, New Zealand.

Sépulveda, F., Andrews, J., Kim, J., Siega, C., & Milloy, S. F. (2015). Spatial-temporal Characteristics of Microseismicity (2009-2014) of the Wairakei Geothermal Field, New Zealand. Paper presented at World Geothermal Congress, Melbourne, Australia.

Sharp, I. R., Gawthorpe, R. L., Underhill, J. R., & Gupta, S. (2000). Fault-propagation folding in extensional settings: Examples of structural style and synrift sedimentary response from the Suez rift, Sinai, Egypt. Geological Society of America Bulletin, 112(12), 1877–1899. http://doi.org/10.1130/0016-7606(2000)112<1877:FPFIES>2.0.CO;2

Sheridan, J. M., & Hickman, S. H. (2004). In situ stress, fracture, and fluid flow analysis in well 38C-9: An enhanced geothermal system in the Coso Geothermal Field. Paper presented at 29th Workshop on Geothermal Reservoir Engineering, Stanford, U.S.A.

Sibson, R. H. (1996). Structural permeability of fluid-driven fault-fracture meshes. Journal of Structural Geology, 18(8), 1031-1042.

Siler, D. L., Faulds, J. E., Mayhew, B., & McNamara, D. D. (2016). Analysis of the favorability for geothermal fluid flow in 3D: Astor Pass geothermal prospect, Great Basin, northwestern Nevada, USA. Geothermics, 60, 1–12. http://doi.org/10.1016/j.geothermics.2015.11.002

Soengkono, S., & Hochstein, M. P. (1992). Magnetic anomalies over the Wairakei geothermal field, central north island, New Zealand. Transactions Geothermal Resources Council, 16, 273–278.

Stagpoole, V. M., & Bibby, H. M. (1999). Residual gravity anomaly map of the Taupo Volcanic Zone. New Zealand. Institute of Geological and Nuclear Sciences.

Stirling, M., McVerry, G., Gerstenberger, M., Litchfield, N., Van Dissen, R., Berryman, K., Barnes, P., Wallace, L., et al. (2012). National seismic hazard model for New Zealand: 2010 update. Bulletin of the Seismological Society of America, 102(4), 1514-1542.

Taupo District Council. (2009). Taupo LiDAR 2008. 09.073.

Terzaghi, R. D. (1965). Sources of error in joint surveys. Geotechnique, 15(3), 287–304. http://doi.org/10.1680/geot.1965.15.3.287

Tingay, M., Reinecker, J. and Müller, B., 2008. Borehole breakout and drilling-induced fracture analysis from image logs. World Stress Map Project, pp.1-8.

Townend, J., Sherburn, S., Arnold, R., Boese, C., & Woods, L. (2012). Three-dimensional variations in present-day tectonic stress along the Australia-Pacific plate boundary in New Zealand. Earth and Planetary Science Letters, 353, 47–59. http://doi.org/10.1016/j.epsl.2012.08.003

Tsuji, T., Ashi, J., & Ikeda, Y. (2014). Strike-slip motion of a mega-splay fault system in the Nankai oblique subduction zone. Earth, 66(1), 120.

Valley, B., & Evans, K. F. (2010). Stress Heterogeneity in the Granite of the Soultz EGS Reservoir Inferred from Analysis of Wellbore Failure (pp. 1–12). Paper presented at the World Geothermal Congress, Bali, Indonesia.

Vasvari, V. (2011). On the applicability of Dual Laterolog for the deter-mination of fracture parameters in hard rock aquifers. Austrian Journal of Earth Sciences, 104(2), 80-89.

Villamor, P., & Berryman, K. (2001). A late Quaternary extension rate in the Taupo Volcanic Zone, New Zealand, derived from fault slip data. New Zealand Journal of Geology and Geophysics, 44(2), 243–269. http://doi.org/10.1080/00288306.2001.9514937

Villamor, P., Clark, K., Watson, M., Rosenberg, M., Lukovic, B., & Ries, W., et al. (2015). New Zealand Geothermal Power Plants as Critical Facilities: An Active Fault Avoidance Study in the Wairakei Geothermal Field, New Zealand. Paper presented at the World Geothermal Congress, Melbourne, Australia.

Villamor, P., Nicol, A., Seebeck, H., Rowland, J., Townsend, D., Massiot, C., et al. (2017a). Tectonic structure and permeability in the Taupō Rift: New insights from analysis of LIDAR derived DEMs. Paper presented at 39th New Zealand Geothermal Workshop, Rotorua, New Zealand.

Villamor, P., Berryman, K. R., Ellis, S. M., Schreurs, G., Wallace, L. M., Leonard, G. S., Langridge, R. M., & Ries, W. F. (2017b). Rapid Evolution of Subduction-Related Continental Intraarc Rifts: The Taupo Rift, New Zealand. Tectonics, 36 (10), 2250-2272.

Wallace, L. M., Beavan, J., McCaffrey, R., & Darby, D. (2004), Subduction zone coupling and tectonic block rotations in the North Island, New Zealand. Journal of Geophysical Research, 109, doi: 10.1029/2004JB003241.

Wallis, I. C., McNamara, D., Rowland, J. V., & Massiot, C. (2012). The nature of fracture permeability in the basement greywacke at Kawerau Geothermal Field, New Zealand. Paper presented at 37th Workshop on Geothermal Reservoir Engineering, Stanford, U.S.A.

Walsh, J. J., & Watterson, J. (1991). Geometric and kinematic coherence and scale effects in normal fault systems. Geological Society, 56(1), 193–203. http://doi.org/10.1144/GSL.SP.1991.056.01.13

Wilson, C. J. N., & Rowland, J. V. (2016). The volcanic, magmatic and tectonic setting of the Taupo Volcanic Zone, New Zealand, reviewed from a geothermal perspective. Geothermics, 59, 1–20. http://doi.org/10.1016/j.geothermics.2015.06.01

Wilson, C. J. N., Houghton, B. F., McWilliams, M. O., Lanphere, M. A., Weaver, S. D., & Briggs, R. M. (1995). Volcanic and structural evolution of Taupo Volcanic Zone, New Zealand: a review. Journal of Volcanology and Geothermal Research, 68(1-3), 1-28.

Wilson, C. J. N., Rogan, A. M., Smith, I. E. M., Northey, D. J., Nairn, I. A., & Houghton, B. F. (1984). Caldera volcanoes of the Taupo volcanic zone, New Zealand. Journal of Geophysical Research: Solid Earth, 89, 8463-8484.

Wood, C. P., Brathwaite, R. L., & Rosenberg, M. D. (2001). Basement structure, lithology and permeability at Kawerau and Ohaaki geothermal fields, New Zealand. Geothermics, 30(4), 461–481. http://doi.org/10.1016/S0375-6505(01)00003-7.

Williams, C.A., Eberhart-Phillips, D., Bannister, S., Barker, D.H., Henrys, S., Reyners, M. & Sutherland, R. (2013). Revised interface geometry for the Hikurangi subduction zone, New Zealand. Seismological Research Letters, 84, 1066-1073.

Wyering, L. D., Villeneuve, M. C., Wallis, I. C., Siratovich, P. A., Kennedy, B. M., Gravley, D. M., & Cant, J. L. (2014). Mechanical and physical properties of hydrothermally altered rocks, Taupo Volcanic Zone, New Zealand. Journal of Volcanology and Geothermal Research, 288, 76–93. http://doi.org/10.1016/j.jvolgeores.2014.10.008

Yoshioka, K., & Stimac, J. (2010). Geologic and Geomechanical Reservoir Simulation Modeling of High Pressure Injection, West Salak, Indonesia (pp. 1–10). Presented at the World Geothermal Congress.

Zhang, X., & Sanderson, D. J. (1996). Numerical modelling of the effects of fault slip on fluid flow around extensional faults. Journal of Structural Geology, 18(1), 109-119.

Zoback, M. D. (2010). Reservoir Geomechanics. Cambridge University Press.

Feature	WK261	WK264	WK266	Feature	WK271
			Natural Features		
Low-amplitude fracture [a]	552 (47)	558 (87)	189 (49)	Conductive Fracture [a]	1617 (438)
High-amplitude fracture [a]	1	2	0	Resistive Fracture [a]	134 (22)
Travel time fractures	97	193	47	Halo Fracture	81
Fault	2	0	0	Fault	7
				Ambiguous Structure	268
			Induced Features [b]		
DITF	91	51	16	DITF	1091
Single DITF	13	0	4	Single DITF	53
Petal centreline fracture	6	2	0	Petal Centreline Fracture	0

[a] Numbers in brackets refer to the number of partial features of that type
[b] No borehole breakouts observed

Table 1. Number of features observed on BHTV and resistivity logs in the study wells.

Strike	Dip Direction	Total Well	WK261	WK264	WK266	WK271

		Fractures (%)				
NE-SW	SE (112.5° - 157.5°)	30 (32)	29 (28)	15 (13)	24 (15)	37 (41)
	NW (292.5° - 337.5°)	14 (12)	21 (22)	16 (17)	16 (23)	12 (6)
E-W	S (157.5° - 202.5°)	16 (18)	12 (13)	15 (15)	10 (8)	17 (22)
	N (337.5° - 022.5°)	11 (8)	11 (10)	22 (20)	9 (11)	6 (4)
NW-SE	SW (202.5° - 247.5°)	7 (9)	6 (7)	5 (6)	3 (4)	9 (10)
	NE (022.5° - 067.5°)	4 (4)	3 (4)	8 (9)	7 (6)	2 (2)
N-S	E (067.5° - 112.5°)	9 (8)	9 (8)	8 (7)	17 (12)	9 (7)
	W (247.5° - 292.5°)	9 (10)	9 (8)	11 (13)	14 (21)	8 (8)

[a] Numbers in brackets are percentages calculated from uncorrected data.

Table 2. Percentage of fractures (corrected for orientation bias) observed on BHTV and FMI logs for each dip direction.[a]

Borehole ID	WK261	WK264	WK266	WK271	WK271 (shallow Interval)	WK271 (deep Interval)	Average of wells WK261, WK264, and WK266 (BHTV)	Average of all wells
Latitude	38° 37'14.941"S	38° 37'5"S	38° 37'14.834"S	38° 36' 58.109" S				
Longitude	176° 2'38.327"E	176° 3'4" E	176° 2'38.694"E	176° 2' 47.515" E				
Azimuth (°)	43.2	46.4	35.4	17.9	7.5	23.1	43	29.5
Feature Type	DITF	DITF	DITF	DITF	DITF	DITF	DITF	DITF
Depth [km.mCHF]	1576	1267.5	859.5	1686	1470.5	1925.5		
Quality	A	B	C	B	B	A	B	B
Date	20110218	20101025	20110403	20131111	20131111	20131111		
n	91	51	16	1091	356	735	158	1249
S. D. (°)	11.9	18.6	13.9	15.5	16.6	11.8	14.5	19.7
Length [m]	102.2	44.5	21.6	197.7	70.4	127.3	168.2	365.9
Top [mrsl]	-628	-977	-199	-702	-702	-1200		
Bottom [mrsl]	-1488	-518	-470	-1556	-1200	-1556		
Top [mCHF]	1146	1038	719	1231	1231	1710		
Bottom [mCHF]	2006	1497	1000	2141	1710	2141		
Top.log [mrsl]	-621	-416	-62	-669	-669	-1200		
Bottom.log [mrsl]	-1523	-1516	-671	-1487	-1200	-1565		
Top log [mCHF]	1139	936	581	1196	1196	1710		
Bottom log [mCHF]	2041	2036	1211	2151	1710	2151		
Well deviation range (mean) [°]	subvertical	subvertical	0-19 (14)	19-24 (20)	19-24 (20)	19-20 (20)		
Well azimuth range (mean) [°]	subvertical	subvertical	92-119 (100)	347-357 (348)	347-457 (348)	347-348 (348)		

Table 3. Stress indicators from the analyzed acoustic borehole images of A–D Quality (based on World Stress Map criteria; Tingay et al., 2008). Azimuth: Interpreted orientation of S_{Hmax}. Number: The amount of recognized feature pairs in a single well (borehole breakouts and drilling induced tensile fractures). S.D.: Standard deviation calculated according to the circular statistics of bi-polar data by Mardia (1972) with a weighting depending of the length (short: L) of the feature. Length: The added length of the fractured borehole sections. Top and Bottom: The depth of the uppermost and lowermost stress indicator found in the borehole. Depth: The mean between top and bottom (mCHF: reference to casing head flange, equivalent to ground level; mrsl: reference to sea level). Date: Date of the tool run. Top.log: depth of the top of the image log. Bottom.log: depth of the bottom of the image log. Well orientation data and S_{Hmax} orientation averages and standard deviations (weighted for DITF length) of the four study wells.

Figure 1. A) Map of the Taupo Volcanic Zone (TVZ) and its major structural elements. Inferred accommodation zones and rift axis (Rowland and Sibson, 2001), active faults (Langridge et al., 2016), TVZ boundary (Wilson et al., 1995), inferred caldera boundaries (Wilson and Rowland, 2016), resistivity boundary zone, Rotokawa; (Risk, 2000), Wairakei; (Risk, 1984). B) Map of the Te Mihi area of the Wairakei Geothermal Field showing structural elements, the locations of the four study wells, and the cross-section line A-A', Figure 2. C) Map of the North Island of New Zealand showing the location of the TVZ and Wairakei.

Figure 2. A) Cross-section from A to A' (location on Figure 1) derived from the 3D geological model of the Wairakei-Tauhara Geothermal Field (Alcaraz, 2014) showing the stratigraphy and structure of the Te Mihi area. Well paths are projected onto the cross-section and their intersection with cross-section faults is schematic. B) Stratigraphic column of the regional geology relevant to the Te Mihi study wells.

Figure 3. A) Example of a travel time fractures from the BHTV logs (green sinusoid), B) Example of a halo structure from the FMI image log (pink sinusoid)

Figure 4. New mapping of active faults within: A) Lake Taupo and Wairakei Geothermal Field; and B) the Te Mihi region of the Wairakei Geothermal Field (area defined by the green box in Figure 4A), and the cross-section line B-B' (Figure 9B). Base maps are hill-shaded reliefs from: LiDAR derived DEM from Waikato Regional Council (Taupo District Council, 2009) in both panels A and B); and from an 8 m pixel DEM in the northern part of panel B (Geographx, 2012).

Figure 5. Diagrams of fracture density, orientation and image quality for wells WK261, WK262, WK266, and WK271. Fracture density for each well is plotted as both the moving average density over 5 m intervals (colored for lithology) and cumulative fracture density (black lines with red portions indicating intervals where fracture density is higher than average well fracture density). Larger stereonets show total well fracture orientations and smaller stereonets show fracture orientations within each lithology in each well. All stereonets are Schmidt net, lower hemisphere, π plots, contoured using Fisher distributions (Grid density = high, Gaussian distribution K parameter = 100, contouring method = Triangulation contouring steps = 250) for data corrected for orientation bias (n = raw, uncorrected fracture count). Image quality for each well is indicated by the greyscale bar charts next to each fracture density plot. Shaded yellow

intervals on the fracture density plots indicates the possible depths at which wells intersect the Kaiapo Fault strands.

Figure 6. Plots of the stress orientations, cumulative density of active structures in each study well (green), the cumulative en échelon DITF density in well WK271 (purple), overlaid with permeable zone locations and possible regional fault intersection intervals.

Figure 7. A) BHTV image of DITF orientation displaced across fractures. B) Interpretation of BHTV image in Figure 7A to clearly show DITF orientation (dashed blue lines) displaced across active fractures (dashed black lines). C) Contoured stereonet of a π plot of active fractures (uncorrected) in all study wells. Green dots = poles to fracture planes, stereonet is lower hemisphere, Fisher contoured.

Figure 8. Plots showing cumulative fracture densities of all fractures in the well, travel time fractures in BHTV logged wells, halo fractures in the FMI logged well, active fractures in all wells, and cumulative fracture aperture of all fractures in all wells, overlaid with permeable zone locations and possible regional fault intersection intervals. Also shown in a greyscale bar chart is image quality, and the stratigraphy of each well colored for lithology. Stereonets are π plots of the orientations of fractures located within the permeable zones of each well (lower hemisphere, Fisher contoured for fracture count corrected for orientation bias, n = corrected fracture count).

Figure 9. Interpreted structural map of: A) Lake Taupo and the western Wairakei Geothermal Field; and B) the Te Mihi region. Regional fault strands are in the same color. Ticks on faults denote the downthrown block (hanging wall). C) Cross-section (B-B’, Figure 9B) showing where projected, mapped faults, dipping 70°, intersect well tracks of the four study wells.

Figure 10. Schematic diagrams of variable morphologies in steeply dipping normal faults that can create variable distributions of antithetic structural orientations.

Figure 11. A) Map of faulting, GNSS vectors (Beavan et al., 2016), and resistivity anomalies of the eastern North Island of New Zealand, B) Conceptual tectonic model of the TVZ highlighting spatial correlations of geothermal expression (resistivity anomalies) and potential zones of localized biaxial extension with intersecting, active, normal, NE-SW and E-W striking faults. Modern and Old Taupo Rift boundary as defined in Villamor et al. (2015).

Figure 1.

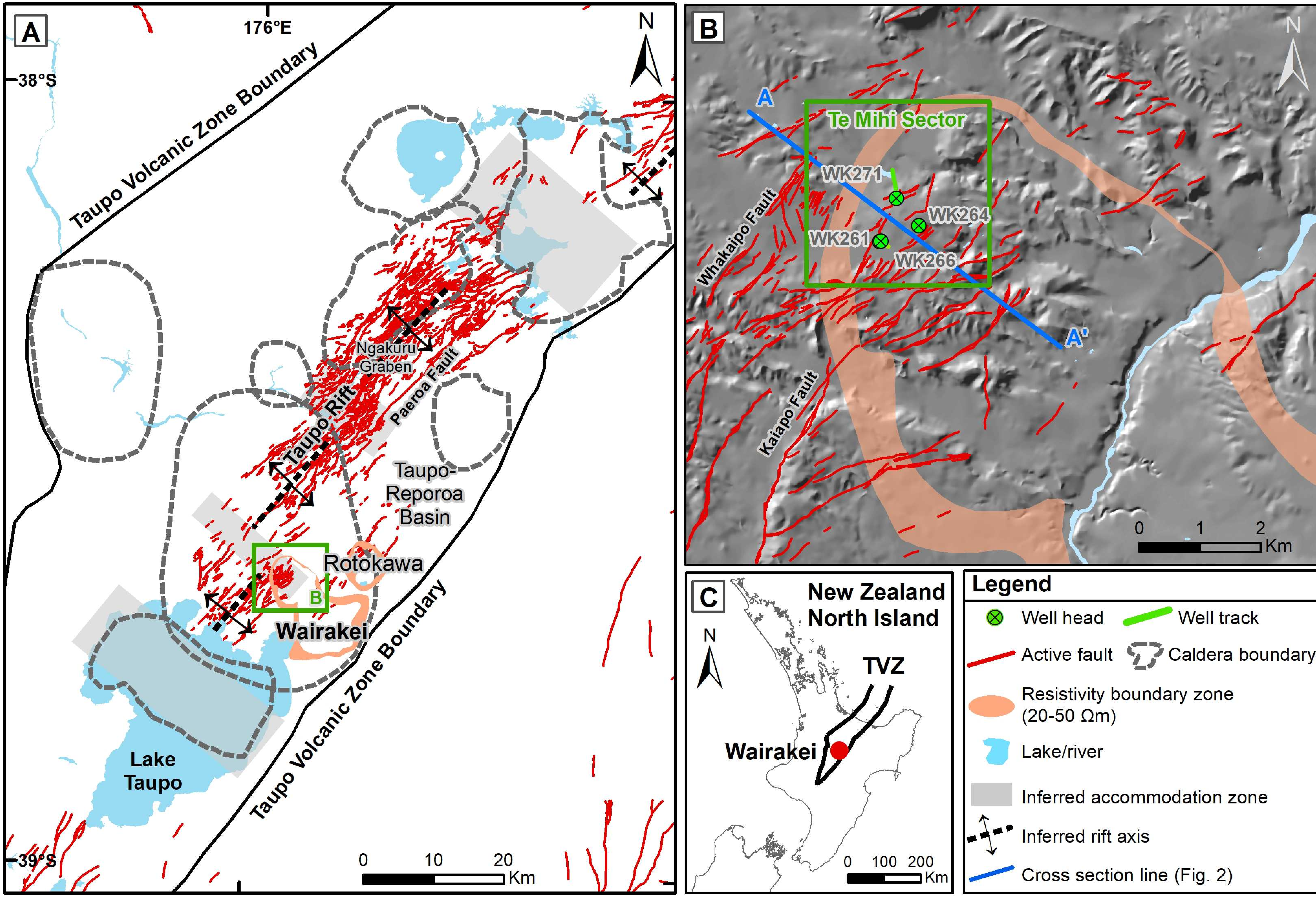
A
176°E
38°S
39°S
N
Taupo Volcanic Zone Boundary
Ngakuru Graben
Paeroa Fault
Taupo Rift
Taupo-Reporoa Basin
Rotokawa
B
Wairakei
Lake Taupo
0 10 20 Km
B
N
A
A'
Te Mihi Sector
WK271
WK264
WK261
WK266
Whakaipo Fault
Kaiapo Fault
0 1 2 Km
C
New Zealand North Island
N
TVZ
Wairakei
0 100 200 Km
Legend
Well head
Well track
Active fault
Caldera boundary
Resistivity boundary zone (20-50 Ωm)
Lake/river
Inferred accommodation zone
Inferred rift axis
Cross section line (Fig. 2)

Figure 2.

A
A
NW
A'
SE
B
Whakaipo Fault zone
Whakaipo Fault zone
Whakaipo Fault zone
Kaiapo Fault zone
Kaiapo Fault zone
WK266
WK261
WK264
WK271
?
?
Depth (mRL)
1000
0
-1000
-2000
-3000
0
1
2
3
4
5
6
Distance (km)
Legend
Superficial deposits
Oruanui Formation
Huka Falls Formation
Fault
Rautehuia breccia
Waiora Formation
Karapiti rhyolite
Uncertain fault
Waiora (Wa1) ignimbrite
Whakamaru Group ignimbrite
Tahorakuri Formation
Projected well track
Poihipi rhyolite
Stockyard ignimbrite
Kaiapo rhyolite complex
WP
WR
WH
TH
P
S
A
K
WP (Waiora Formation): Intercalated fine-grained tuffs, silicified sandstone, siltstone, and mudstone.
Tuffs are non-welded to weakly welded.
Waiora (Wa1) ignimbrite (WK266) is a moderately to densely welded, crystal and pumice-rich ignimbrite.
WR (Waiora rhyolites):
WK271 - A porpyritic rhyolite with a micro-spherulitic groundmass which is locally flow-banded.
WK266 - Karapiti 2B rhyolite - weakly porphyritic, pumice-bearing rhyolite lava and breccia, weakly flow-banded.
WH (Whakamaru Group ignimbrite):
Partially welded to unwelded, crystal rich ignimbrite.
TH (Tahorakuri Formation): Partially- to unwelded tuffs and breccias.
P (Poihipi rhyolite): Weakly porphyritic, flow-banded and spherulitic rhyolite lava, with a brecciated carapace.
S (Stockyard ignimbrite): Strongly welded ignimbrite.
A (Andesite intrusion): Porphyritic andesite with plagioclase phenocrysts.
K (Kaiapo rhyolite complex): Porphyritic rhyolite lavas with a variably spherulitic groundmass.

Figure 3.

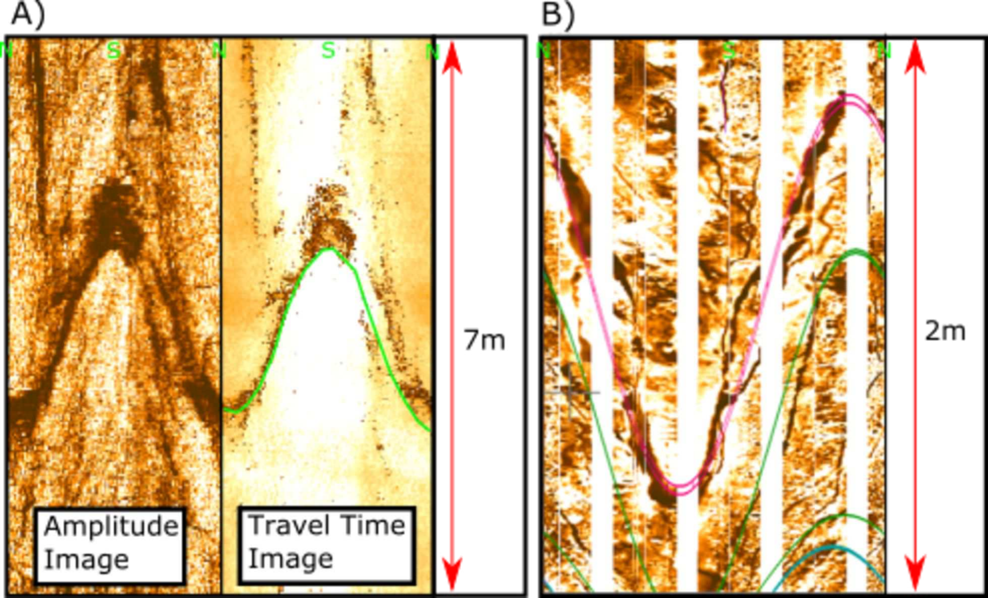

A)
B)
N
S
N
N
S
N
N
S
N
7m
2m
Amplitude Image
Travel Time Image

Figure 4.


A
N
Orakonui Fault
Aratiatia Fault
Whakaipo Fault
Kaiapo Fault
B
Lake Taupo
0
3
6
Km
B
N
WK271
B
WK264
WK261
WK266
B'
0
1
2
Km
Legend
Well head
Well track
Resistivity boundary zone
(20-50 Ωm)
Lake/river
Cross section line (Fig. 9)
Active fault:
down quadrant NE, E, SE, S
Active fault:
down quadrant N, NW, SW, W
Active fault:
all others not re-mapped

Figure 5.

WK261
WK266
WK264
WK271
Density/5 m
Cumulative density
Depth (m.r.s.l.)
full imaged interval
n=699
n=285
n=840
n=2567
N
SHmax
Kaiapo Fault
Waiora Formation
Wairakei ignimbrite
Tahorakuri Formation
Kaiapo rhyolite
Karapiti 2B rhyolite
Waiora (Wa1) ignimbrite
Pohipi rhyolite
And. in
Tah. Fm.
Stock. ig.
rhyolite
n=115
n=68
n=286
n=230
n=114
n=93
n=10
n=257
n=225
n=141
n=181
n=26
n=253
n=295
n=805
n=543
n=671
Lithology
Non-welded ignimbrite
Partially-welded ignimbrite
Welded ignimbrite
Rhyolite
Andesite
Stereonet density
high
low
% Image interpretable
0%
25%
50%
75%
100%

Figure 6.


WK266
Azimuth (°)
WK264
Azimuth (°)
WK261
Azimuth (°)
WK271
Azimuth (°)
Depth (m.r.s.l.)
Cumulative active structures
Cumulative en echelon DITF
Kaiapo Fault
Waiora Formation
Karapiti 2B rhyolite
Waiora (Wa1) ignimbrite
Whakamaru Group ig.
Tahorakuri Formation
Kaiapo rhyolite
Pohipi rhyolite
And. in
Tah. Fm.
Stock. ig.
rhyolite
Whakamaru Group ignimbrite
Drilling induced tensile fractures
Single drilling induced tensile fractures
Petal centerline fractures
Permeable zone
Approximate fault intersection
Mean SHmax
Mean SHmin
SHmax standard deviation
SHmin standard deviation
Cumulative active structures
Active structure - WK266
Cumulative en echelon DITF in WK271
Lithology
Non-welded ignimbrite
Partially-welded ignimbrite
Welded ignimbrite
Rhyolite
Andesite
% Image interpretable
0%
25%
50%
75%
100%

Figure 7.

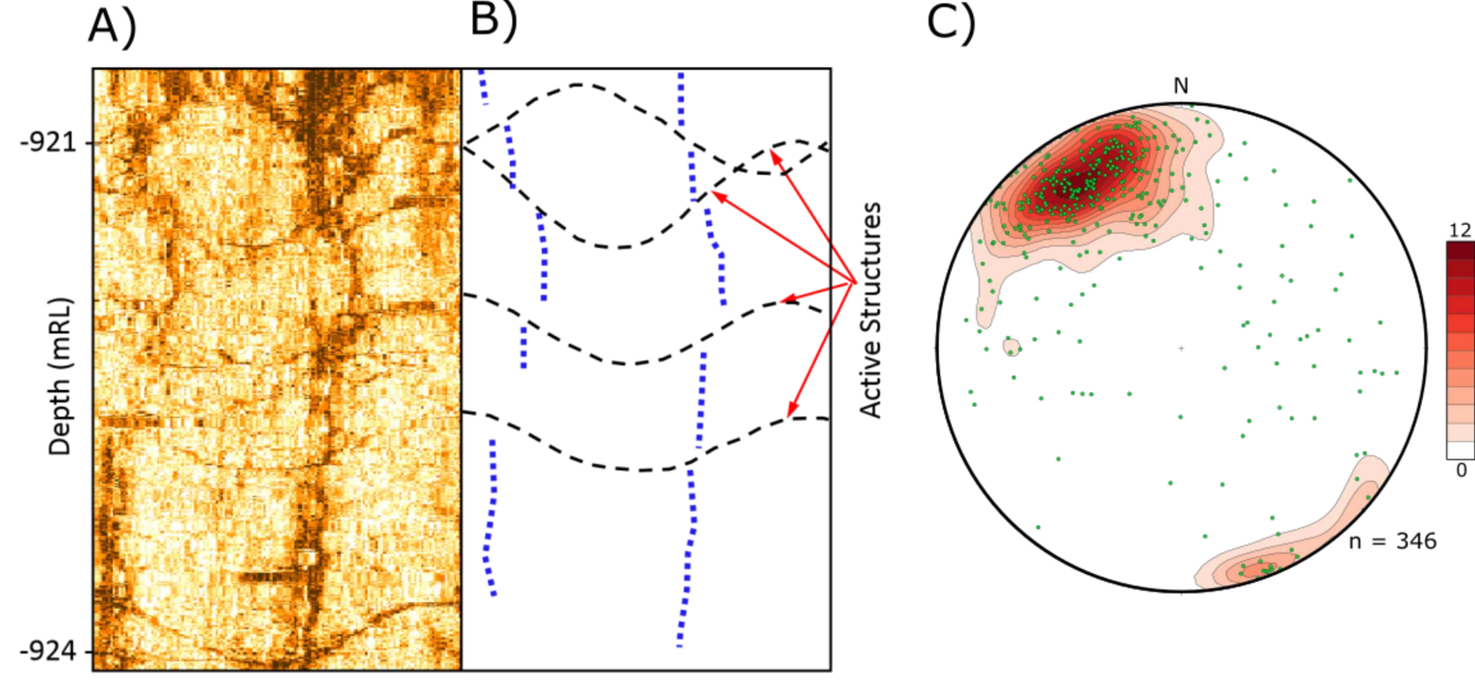

A)
B)
C)
-921
-924
Depth (mRL)
Active Structures
N
n = 346
12
0

Figure 8.

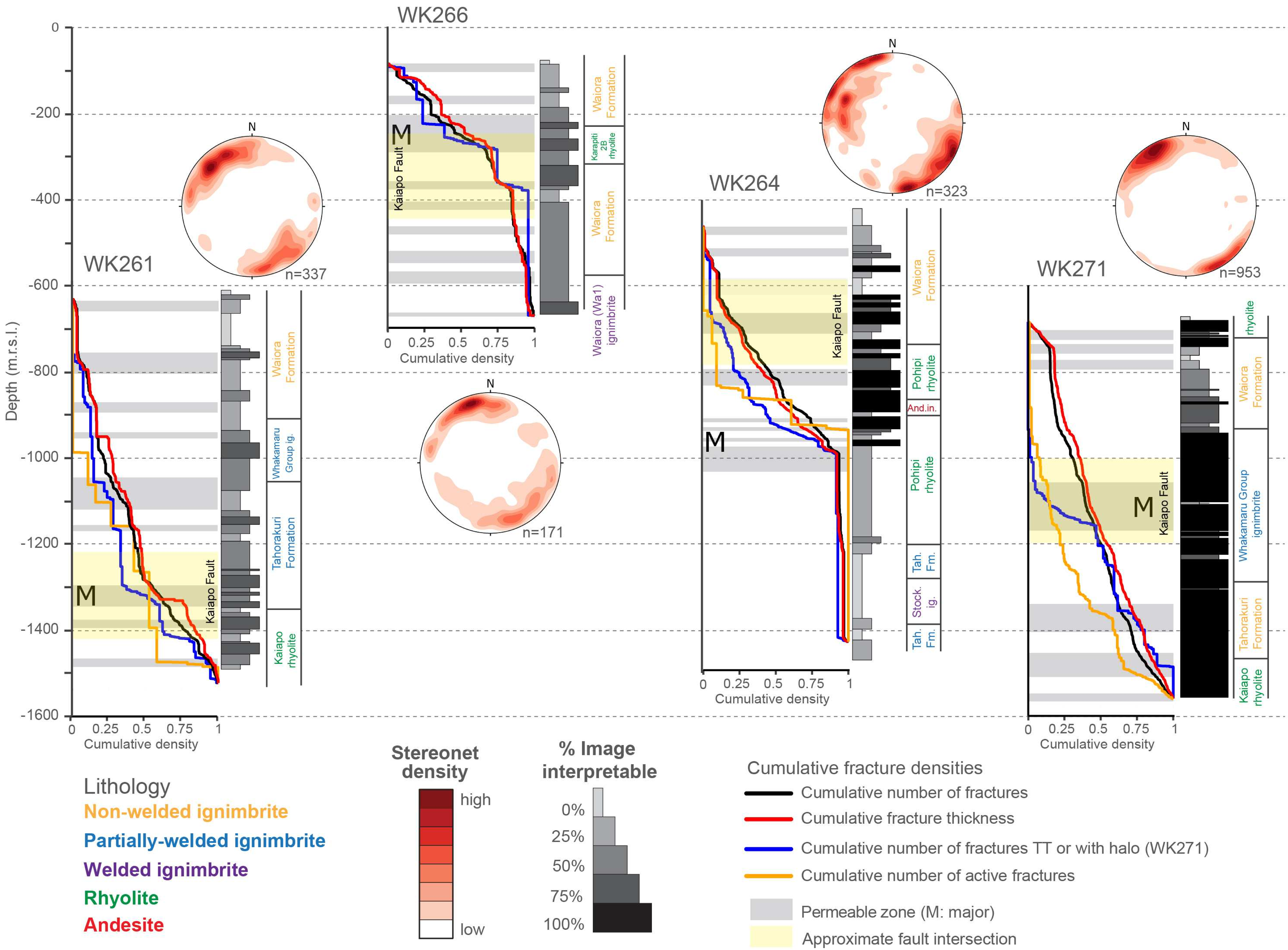

WK261
WK266
WK264
WK271
Depth (m.r.s.l.)
Cumulative density
Kaiapo Fault
M
n=337
n=171
n=323
n=953
Waiora Formation
Whakamaru Group ig.
Tahorakuri Formation
Kaiapo rhyolite
Karapiti 2B rhyolite
Waiora (Wa1) ignimbrite
Pohipi rhyolite
And.in.
Tah. Fm.
Stock. ig.
rhyolite
Whakamaru Group ignimbrite
Lithology
Non-welded ignimbrite
Partially-welded ignimbrite
Welded ignimbrite
Rhyolite
Andesite
Stereonet density
high
low
% Image interpretable
0%
25%
50%
75%
100%
Cumulative fracture densities
Cumulative number of fractures
Cumulative fracture thickness
Cumulative number of fractures TT or with halo (WK271)
Cumulative number of active fractures
Permeable zone (M: major)
Approximate fault intersection

Figure 9.

A
N
0 1 2
Km
Lake Taupo
B
B
N
WK271
WK264
WK261
WK266
B
B'
0 1
Km
C
B
NW
B'
SE
WK271
WK261
WK266
WK264
1000
500
0
-500
-1000
-1500
-2000
Depth (mRL)
0
1
2
3
Distance (km)
Key
Fault
Well track
Minor permeable zone
Major permeable zone
These strands of the Kaiapo
Fault likely merge at depth
Legend
Well head
Well track
Resistivity boundary zone (20-50 Ωm)
Lake/river
Cross section line
Whakaipo Fault
Kaiapo Fault
Ngangiho Fault
Karapiti Fault
Wairakei Fault
Orakonui Fault
Crater Moon Fault
Te Mihi Fault
Ngangautu Fault

Figure 10.

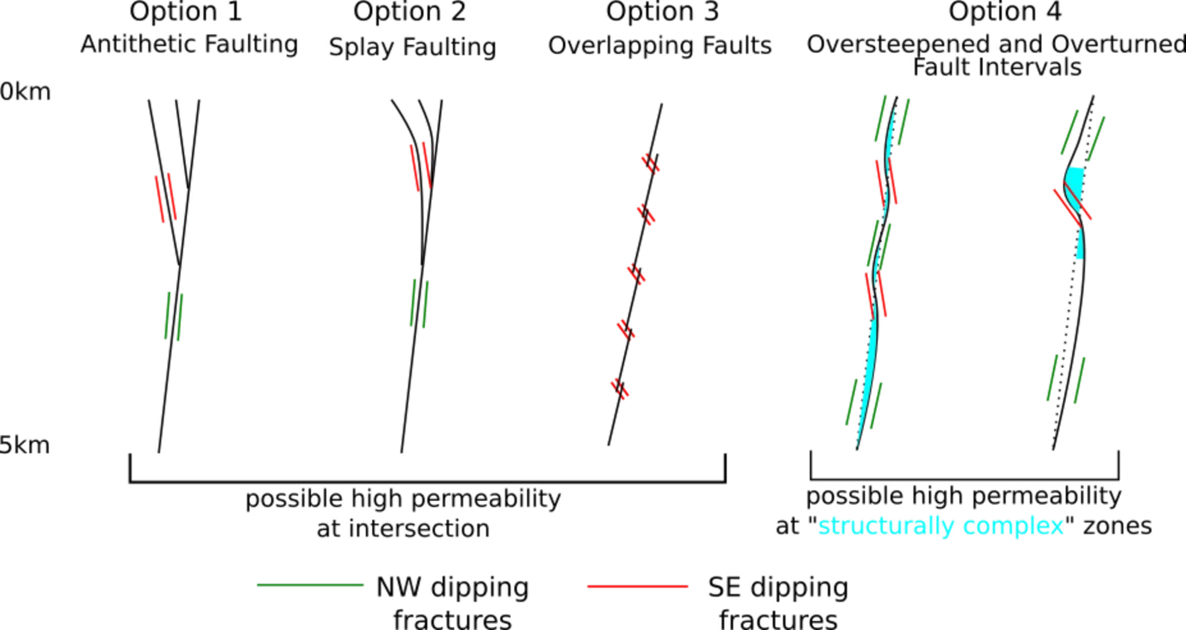
Option 1
Antithetic Faulting
Option 2
Splay Faulting
Option 3
Overlapping Faults
Option 4
Oversteepened and Overturned Fault Intervals
0km
5km
possible high permeability at intersection
possible high permeability at "structurally complex" zones
NW dipping fractures
SE dipping fractures

Figure 11.

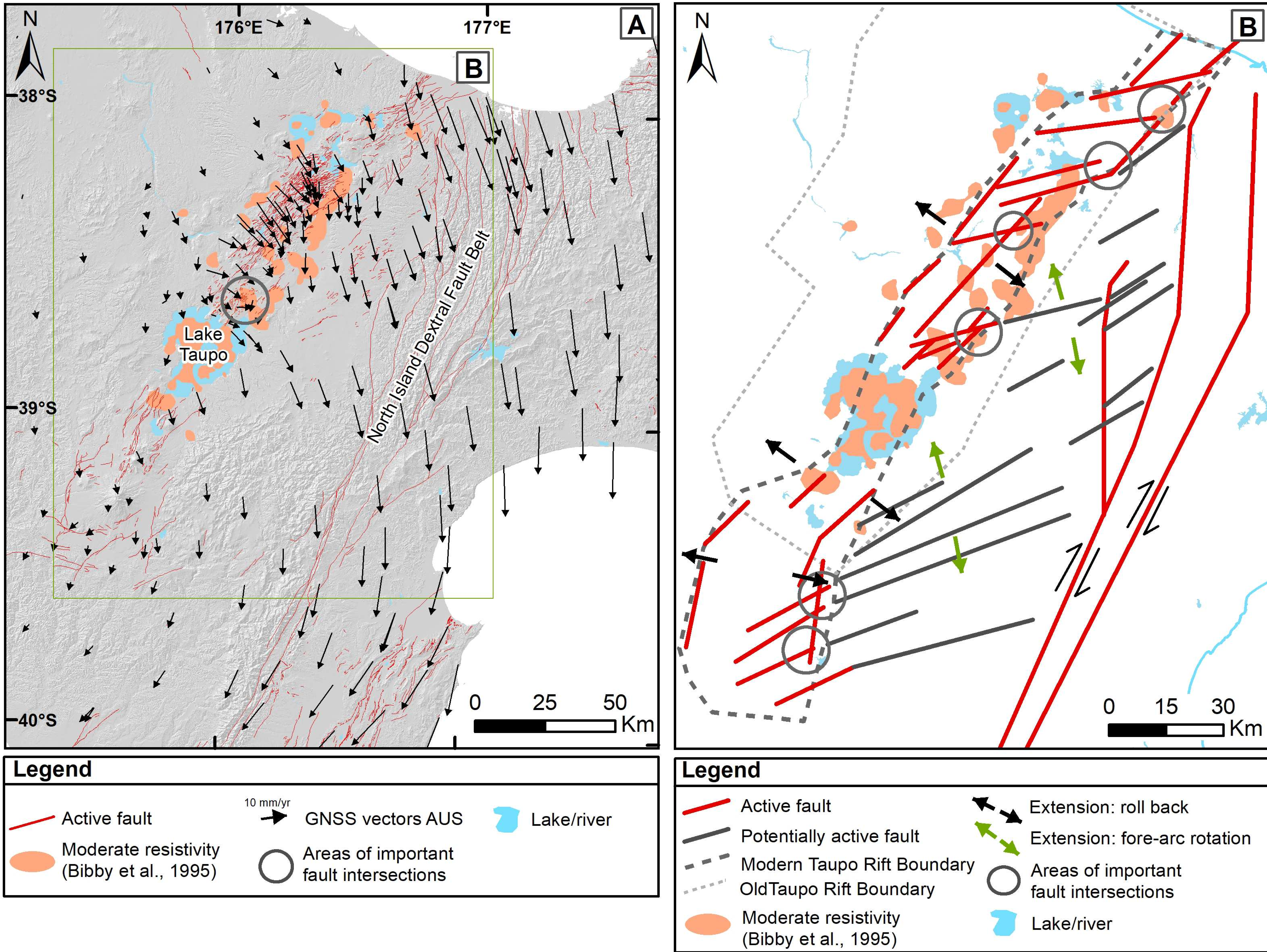
N
176°E
177°E
A
B
38°S
39°S
40°S
Lake Taupo
North Island Dextral Fault Belt
0 25 50
Km
Legend
Active fault
10 mm/yr
GNSS vectors AUS
Lake/river
Moderate resistivity (Bibby et al., 1995)
Areas of important fault intersections
N
B
0 15 30
Km
Legend
Active fault
Potentially active fault
Modern Taupo Rift Boundary
OldTaupo Rift Boundary
Moderate resistivity (Bibby et al., 1995)
Extension: roll back
Extension: fore-arc rotation
Areas of important fault intersections
Lake/river